

# Feasibility of melt segregation from a crystal mush in response to the 2011–2012 eruption at Cordón Caulle, Chile

Patrick R. Phelps<sup>1,2</sup>, Helge M. Gonnermann,<sup>1</sup> Heather Winslow,<sup>3</sup> Philipp Ruprecht,<sup>3</sup> Matthew E. Pritchard,<sup>4</sup> Francisco Delgado<sup>5</sup> and Yang Liao<sup>6</sup>

<sup>1</sup>Rice University, Department of Earth, Environmental and Planetary Sciences, 6100 Main St., Houston, TX 77005, USA, E-mail: [patrick.phelps@ucalgary.ca](mailto:patrick.phelps@ucalgary.ca).

<sup>2</sup>University of Calgary, Department of Geoscience, 2500 University Drive N.W., Calgary, AB T2N1N4, Canada

<sup>3</sup>University of Nevada, Reno, Department of Geological Sciences and Engineering, 1664 N. Virginia St., Reno, NV 89557, USA

<sup>4</sup>Cornell University, Department of Earth and Atmospheric Sciences, 616 Thurston Ave. Ithaca, NY 14853, USA

<sup>5</sup>Universidad de Chile, Departamento de Geología, 8370415 Santiago, Chile

<sup>6</sup>Woods Hole Oceanographic Institute, Department of Geology and Geophysics, 86 Water St., Falmouth, MA 02543, USA

Accepted 2023 June 22. Received 2023 June 19; in original form 2022 October 28

## SUMMARY

The 2011–2012 eruption at Cordón Caulle in Chile produced crystal-poor rhyolitic magma with crystal-rich mafic enclaves whose interstitial glass is of identical composition to the host rhyolite. Eruptible rhyolites are thought to be genetically associated with crystal-rich magma mushes, and the enclaves within the Cordón Caulle rhyolite support the existence of a magma mush from which the erupted magma was derived. Moreover, towards the end of the 2011–2012 eruption, subsidence gave way to inflation that has on average been continuous through at least 2020. We hypothesize that magma segregation from a crystal mush could be the source of the observed inflation. Conceptually, magma withdrawal from a crystal-poor rhyolite reservoir caused its depressurization, which could have led to upward flow of interstitial melt within an underlying crystal mush, causing a new batch of magma to segregate and partially recharge the crystal-poor rhyolite body. Because the compressibility of the crystalline matrix of the mush is expected to be lower than that of the interstitial melt, which likely contains some fraction of volatile bubbles, this redistribution of melt would result in a net increase in volume of the system and in the observed inflation. We use numerical modelling of subsurface magma flow and storage to show under which conditions such a scenario is supported by geodetic and petrologic observations.

**Key words:** Numerical modelling; Magma chamber processes; Physics of magma and magma bodies.

## 1 INTRODUCTION

Surface uplift is a phenomenon observed at many active volcanoes around the world (e.g. Biggs & Pritchard 2017). It may be due to magma movement underground, including episodes of renewed magma *supply* or *recharge* to subsurface reservoirs (e.g. Delaney & McTigue 1994; Dvorak & Dzurisin 1997; Dzurisin *et al.* 2006). Although we do not understand these processes with certainty, we can use geodetic observations to make inferences about the state of magma storage reservoirs as well as associated magma supply or recharge. The nature of this deeper magma supply process, however, often remains obscure, non-unique and therefore treated in a highly idealized manner.

Our study focuses on inflationary surface deformation during the past decade at Cordón Caulle volcano in Chile (Delgado *et al.* 2016, 2018; Delgado 2021). Cordón Caulle is of particular interest

because it has erupted crystal-poor rhyolite and contains evidence of an active crystal mush through the presence of crystal-rich mafic enclaves within the erupted rhyolite. The enclaves have a glassy matrix of identical composition to the erupted crystal-poor rhyolite (Winslow *et al.* 2022). It has therefore been inferred that the erupted rhyolite represents melt that segregated from an underlying crystal mush, as is envisaged for the *rhyolite-melt crystal mush model* (Bachmann & Bergantz 2004; Hildreth 2004; Hildreth & Wilson 2007). Cordón Caulle, whose eruptions are undoubtedly fed from a crystal-poor rhyolite reservoir, represents a volcanic system where the potential existence of a crystal mush can be tested against observations of inflationary deformation. Specifically, one can test whether the observed inflation could be the consequence of recharge of the crystal-poor rhyolite by melt segregation from an underlying crystal mush.

The rhyolite-melt crystal mush model is part of a conceptual model for lithospheric magmatism wherein asthenosphere derived

basalt feeds transcrustal magmatic systems in which fractionation and hybridization processes eventually produce rhyolite melts at shallow crustal levels (Hildreth 1981), in essence similar to present views of transcrustal magma transport and storage systems (e.g. Annen *et al.* 2006; Bachmann & Huber 2016; Cashman *et al.* 2017; Sparks *et al.* 2019). Although crystal-melt fractionation is believed to take place over a wide range of depths, it is thought that the temporal persistence and growth of such systems leads to elevated upper-crustal geothermal gradients that favour the formation of shallow bodies of high-silica rhyolite-melt by step-wise extraction by porous flow from underlying crystal mushes (Hildreth 2004; Hildreth & Wilson 2007; Huber *et al.* 2019).

No evidence for the existence of such a transcrustal system currently exists at Cordón Caulle and considering how primitive the enclaves from the 2011–2012 eruption are, fractionation processes at Cordón Caulle may be restricted to relatively shallow depths (Winslow *et al.* 2022). Nevertheless, the enclaves do point to the existence of a crystal mush, perhaps at relatively shallow depths and limited vertical extent. Here we assess whether the inflation at Cordón Caulle during the past decade can be reconciled with melt segregation from such a crystal mush body.

We do so using a numerical model for magma transport and storage that is based on the framework of poroelasticity (e.g. Biot 1941; Rice & Cleary 1976; Wang 2000; Cheng 2016), which has been proposed to describe the mechanics occurring within a magma mush over shorter timescales than viscous or plastic deformation processes associated with compaction (Gudmundsson 2012; Liao *et al.* 2018; Mullet & Segall 2022). Hereby the crystal-rich mush is treated as a porous, elastically deforming medium with interstitial melt. The model simulates how the decrease in pressure of the crystal-poor rhyolite reservoir, caused by eruptive magma withdrawal, led to upward flow of interstitial melt within the underlying crystal mush, resulting in recharge of the crystal-poor rhyolite and thus the observed inflation. We use the model to estimate the parameters under which it can reproduce the observed surface deformation and assess the extent to which they support the existence of a magma mush system beneath Cordón Caulle.

## 2 CORDÓN CAULLE

### 2.1 Geological setting

Cordón Caulle is part of the Puyehue-Cordón Caulle volcanic complex (PCC), located within the Andean Southern Volcanic Zone (Fig. 1(a); Singer *et al.* 2008). PCC is a long lived system which has produced  $\approx 7 \text{ km}^3$  of erupted material in the past 16.5 ka. Cordón Caulle is situated within a NW trending graben in the complex, and has produced three eruptions during the past century, in 1921–1922 and 1960 with eruptive vents along graben-bounding faults, and in 2011–2012 (Fig. 1b). All three eruptions were rhyolitic to dacitic and homogeneous in composition (Castro *et al.* 2013; Singer *et al.* 2008), suggesting that they were tapping different parts of a compositionally zoned magma storage system that is either contiguous or compartmentalized with some degree of interconnection, as indicated by spatiotemporal patterns of surface deformation (Jay *et al.* 2014; Delgado 2021).

### 2.2 The 2011–2012 eruption

On 4 June 2011, Cordón Caulle began erupting with a 3–4-d-long Plinian to subplinian phase, with ash reaching 9–12 km, and a volcanic explosivity index (VEI) of 4–5 (Jay *et al.* 2014; Bonadonna *et al.* 2015b). During the following week the ash plume decreased to 4–9 km in height (Bonadonna *et al.* 2015b), and on June 15 crystal-poor rhyolitic lava began extruding from the vent, along with continued ash venting (Crozier *et al.* 2022). Seismic tremors ceased, possibly signalling the end of the eruption on 15 March 2012 (Tuffen *et al.* 2013). The exact end date is, however, obscured since the lava flow field continued to evolve for months (Bertin *et al.* 2012, 2015; Tuffen *et al.* 2013; Coppola *et al.* 2017). Thus, the eruption may have effectively ended by May 2012, when estimated lava discharge rates declined to  $< 5 \text{ m}^3 \text{ s}^{-1}$  (Coppola *et al.* 2017). In total, approximately  $1.5 \text{ km}^3$  dense rock equivalent (DRE) of tephra and lava were extruded over the course of the eruption, with nearly  $1 \text{ km}^3$  erupting explosively within the first few days, and the lava flow making up the remaining  $\sim 0.5 \text{ km}^3$  (Pistolesi *et al.* 2015; Castro *et al.* 2016; Delgado *et al.* 2019; Delgado 2021). Finally, a shallow ( $< 200 \text{ m}$ ) laccolith of  $\sim 0.8 \text{ km}^3$  also intruded syn-eruptively (Castro *et al.* 2016), bringing the total volume of magma withdrawn from the Cordón Caulle magma storage reservoir to  $> 2 \text{ km}^3$ . This ultimately resulted in the deflationary deformation shown in Fig. 1(c), which was preceded and followed by inflationary deformation, all of which will be discussed in more detail in Section 2.4.

### 2.3 Magma storage hypothesis for Cordón Caulle

The 2011–2012 lava is a crystal-poor rhyolite (Castro *et al.* 2013; Jay *et al.* 2014; Seropian *et al.* 2021) containing  $\ll 1$  volume per cent of mafic enclaves (Winslow *et al.* 2022). These mafic enclaves have been interpreted to be pieces of crystal mush which contain interstitial rhyolite melt (Winslow *et al.* 2022). The enclaves range in size from 2 to 20 cm and are comprised of 55–70 per cent interlocking crystals with the remainder as interstitial glass and vesicles (see Fig. 2). The enclaves' bulk composition is basaltic, due to an abundance of olivine, clinopyroxene and plagioclase crystals, as well as minor amounts of Fe–Ti oxides. The interstitial glass of the enclaves has an identical composition to that of the crystal-poor host rhyolite. This fact, together with their crystallinity has led to the interpretation that most of the enclaves are pieces of a crystal mush that is spatially and genetically associated with the crystal-poor rhyolite body from which the 2011–2012 magma erupted. A possible scenario that would be consistent with the prevalent view of how crystal-poor rhyolite is formed (Bachmann & Bergantz 2004; Hildreth 2004) would be a crystal mush overlain by crystal-poor rhyolite with the former somehow being incorporated into the rhyolite flowing towards the eruption-feeding dike or conduit (Hermes & Cornell 1981; Winslow *et al.* 2022).

It should be noted that a small fraction of the enclaves have porphyritic textures, low crystallinity, plagioclase with disequilibrium textures, abundant microlites and a narrow range in mineral chemistry, all of which point towards these enclaves coming from direct mafic injection into the rhyolite layer (Winslow *et al.* 2022). Their abundance is low, and it is unclear whether or to what extent their injection could be the cause of the inflationary deformation prior to the eruption and perhaps the eruption itself. Because the objective of our analysis is to test the possibility that the inflationary deformation following the eruption is due to melt segregation from a crystal mush, we assume that this deformation is not caused

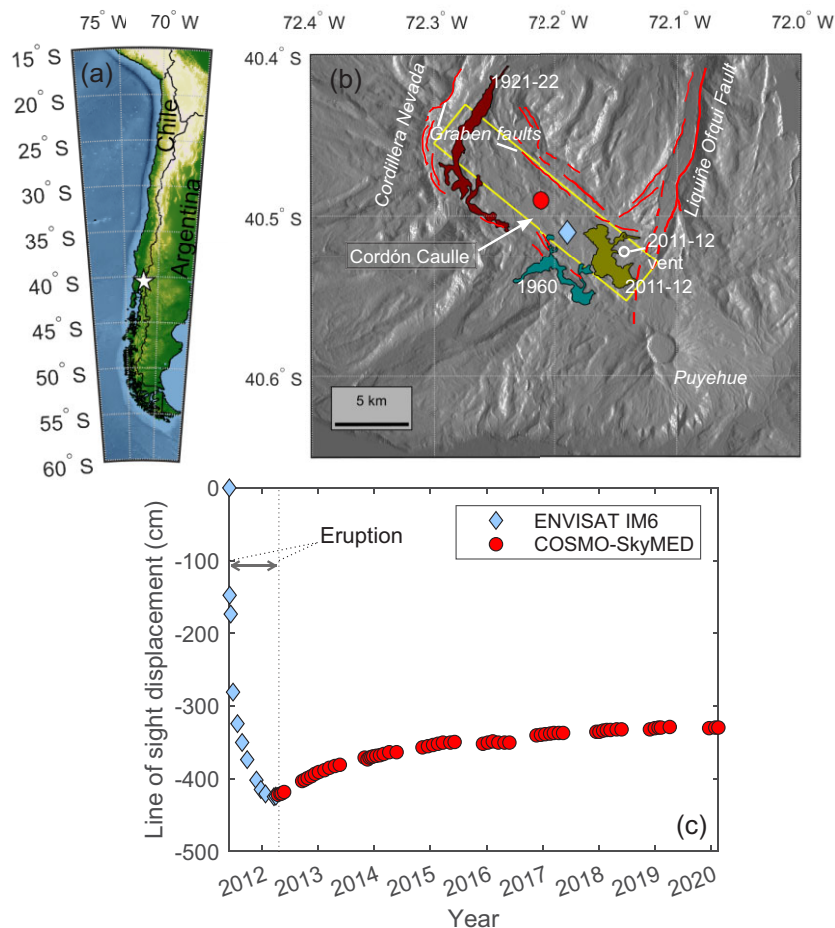


**Figure 1.** (a) Location of the Puyehue-Cordón Caulle volcanic complex (PCC), indicated by the white star. (b) Structural and volcanic features of PCC. Recent lava flows are shown in red (1921–1922), blue (1960) and green (2011–2012). Approximate locations of faults, based on Lara *et al.* (2006) and Delgado (2021), are shown as red lines. Symbols indicate the locations of the line of sight (LOS) displacements from Delgado (2021), which are shown in (c). The red circle indicates the location of the post-eruptive LOS displacement estimates. The yellow box denotes the location and size of the sill used in our model. (c) LOS displacement time-series used as a proxy for overall inflationary and deflationary deformation at Cordón Caulle. Each value shown represents the maximum LOS displacement (Delgado *et al.* 2016) between separate satellite transits and thus combines data from different orbits and viewing geometries. Different symbols correspond to the LOS locations shown in (b). Vertical dashed line indicates end of the eruption.

by renewed mafic injection. We acknowledge, however, that this possibility cannot be ruled out based on the available information.

## 2.4 Ground deformation

Over the course of the eruption approximately 4.25 m of deflation was observed at Cordón Caulle (Delgado 2021), using interferometric synthetic aperture radar (InSAR). Some spatiotemporal variability aside, deflation was essentially centred within the Cordón Caulle graben (Jay *et al.* 2014; Delgado 2021; Novoa *et al.* 2022) and was consistent with magma withdrawal from a shallow magma body located within the graben (Delgado *et al.* 2019). Using a temporal sequence of interferograms, Delgado *et al.* (2019) found the line of sight (LOS) displacements near the centre of the graben. The resultant time-series of LOS displacements captures the temporal evolution of co-eruptive subsidence (blue diamond, Figs 1b and c). Uncertainties exist due to lack of coherence between interferograms during the eruption and the spatiotemporal variability in the location of maximum deflation. They can, however, still be used as a

proxy for the relative rate of change in volume (pressure) within the magma reservoir.

Following the eruption there has been near continuous uplift at Cordón Caulle, also approximately centred within the graben and with relatively limited spatiotemporal variability (Delgado *et al.* 2018; Delgado 2021). This uplift has been interpreted to be the consequence of magma recharge into the reservoir from below (Delgado *et al.* 2016, 2018; Novoa *et al.* 2022), although alternate interpretations may be feasible (e.g. Segall 2016). After analysing the post-eruptive interferograms, Delgado *et al.* (2016) produced a time-series of inflationary LOS displacements from a single location within the graben (red circle, Figs 1b and c), which also can be used as a proxy for the relative rate of change in volume (pressure) within the magma reservoir. Although these data are given for a single location, the maximum deformation has shifted position around this average location. We also note that gradual inflation was occurring prior to the eruption at a slower rate and smaller magnitude than has been observed since the eruption (Delgado *et al.* 2018; Delgado 2021). The exact cause of this pre-eruptive inflation is unknown, but may have been related to deep-seated recharge.

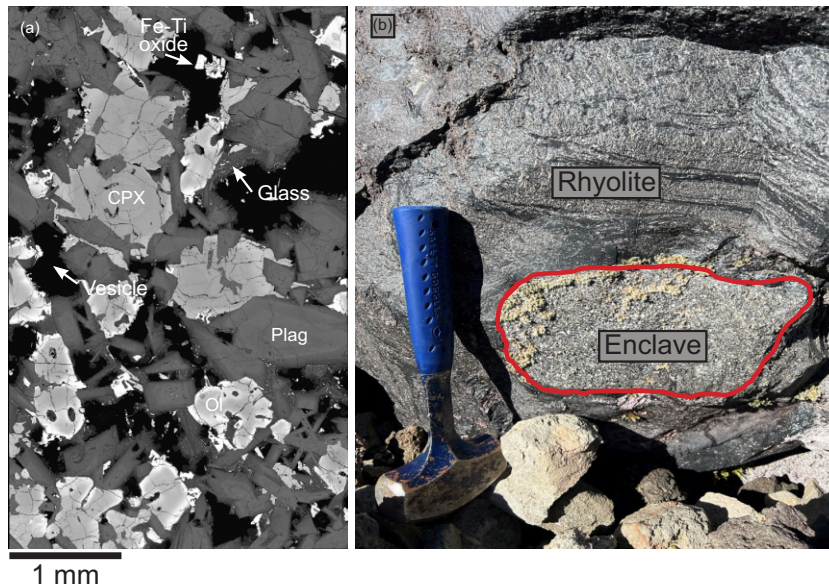


**Figure 2.** Enclaves at the crystal and field scale. (a) Crystal scale image of an enclave modified from Winslow *et al.* (2022). It shows the interlocking crystal texture with vesicles (black areas labelled as ‘Vesicle’) and interstitial glass (‘Glass’). The latter comprises about 4 volume per cent of the enclaves and is difficult to distinguish from plagioclase (‘Plag’), but tends to rim vesicles. Combined glass and vesicles constitute about 36 volume percent of the enclaves. Lighter coloured grains are clinopyroxene (‘CPX’) and olivine (‘Ol’). Fe–Ti oxides are small white grains (‘Fe–Ti oxide’). (b) Field scale image of an enclave within the rhyolite.

The LOS displacement data, recorded for a variety of satellite orbits, viewing geometries and slight spatiotemporal variations in maximum displacement, are scaled to provide a continuous time-series as explained in Delgado (2021), to make the eruptive deflation continuous with the post-eruptive inflation (Fig. 1). For the purposes of our analysis, we treat the LOS displacements as a proxy for the rate of magma withdrawal and resultant change in pressure of the shallow magma reservoir that fed the 2011–2012 eruption. Although this proxy may not strictly describe the maximum deformation over this time span at Cordón Caulle, it provides a sufficient proxy to compare against to test whether the inflationary deformation was caused by melt segregation from a crystal mush.

### 3 THE CONCEPTUAL MODEL

Our objective is to understand the inflationary deformation at Cordón Caulle following the 2011–2012 eruption. In particular, we are interested in assessing whether the observed deformation could be due to melt segregation from a crystal mush, as it is envisioned within the magma mush hypothesis for the formation of eruptible crystal-poor rhyolite (Bachmann & Bergantz 2004; Hildreth & Wilson 2007; Cashman *et al.* 2017). To this end, we developed a mathematical model that describes the poroelastic response of a crystal-rich magma mush to withdrawal of magma from an overlying layer of crystal-poor rhyolite that is contiguous with the mush. The system is presumed to exist within an elastically deformable host rock whose deformation is calculated using the conventional semi-analytical model for the opening of a sill-like dislocation (Okada 1992), which has been shown to provide a reasonable approximation to deformation at Cordón Caulle (Delgado *et al.* 2016). We emphasize that the conceptual model of our system comprises the magma mush plus an overlying sill of rhyolite melt. Rhyolite melt can be removed from this system due to eruption, which will result in a change in magma volume. We approximate the system as closed to magma recharge from below the mush.

The aforementioned porphyritic enclaves, which are interpreted to be a consequence of injection of mafic magma, do allow for the possibility that inflation at Cordón Caulle is due to the injection of magma from below the system. Although they are volumetrically insignificant in the erupted products, it is possible they make up a larger, trapped fraction in the mush. Moreover, the existence of the magma mush is of course contingent upon deep mafic recharge over time. The possibility of direct recharge from a deeper source through a dike or conduit has already been investigated by Delgado *et al.* (2016, 2018), who found that an input of  $0.15 \text{ km}^3$  into the sill through 2017 could produce the uplift. We therefore limit our analysis to the end-member case of recharge due to melt segregation from a magma mush in order to assess solely the extent to which the inflationary deformation during the past decade can be explained by this process.

We assume that the crystal mush acts as a porous medium, where the crystals constitute the porous matrix and the interstitial rhyolite melt is the pore fluid. The pressure within the overlying rhyolite acts as a pressure boundary condition on the mush. Pressure within the overlying rhyolite can change either due to magma withdrawal during eruption or due to magma addition from the underlying mush. A decrease in pressure of the overlying rhyolite, due to eruptive withdrawal, will induce pressure gradients in the interstitial melt that deviate from static, thereby inducing flow of interstitial melt within the mush. This results in a net flow of interstitial melt out of the mush into the overlying rhyolite.

If the resultant change in interstitial melt content were solely due to the compressibility of the interstitial melt, which would be the case for a completely rigid and undeformable crystal matrix, the volume of interstitial melt added or removed from the mush would be associated with no change in volume of the mush itself. On the other hand, if a change in interstitial melt content were solely due to the deformation of the crystal matrix, which would be the case if the interstitial melt is incompressible, then the volume of interstitial melt removed from the mush would be entirely compensated by

a corresponding change in volume of the mush. In reality, any change in interstitial melt content is due to both melt compressibility and matrix deformation, where compressibility of the interstitial melt is due to exsolution and decompression of volatiles (Sparks & Cashman 2017). As a consequence, a redistribution of melt between mush and overlying rhyolite will result in a change in volume of the system. Moreover, the less deformable the crystal matrix, the larger the change in the volume of the system.

The theoretical framework of poroelasticity (e.g. Biot 1941; Rice & Cleary 1976; Wang 2000; Segall 2010; Cheng 2016; Liao *et al.* 2018) describes these principles. A change in volume of the mush therefore requires deformation of the crystal matrix, which is assumed to be instantaneous and fully recoverable. At the same time, the flow of interstitial melt follows Darcy's law and is time-dependent. The flow can be described by a diffusion equation for pore pressure. As a consequence, an instantaneous change in pressure of the overlying rhyolite will result in the gradual diffusion of interstitial melt pressure throughout the mush, with any local volume change of the crystal matrix instantaneously conforming to the local change in interstitial melt pressure.

The model framework is applicable for relatively small mush melt extraction amounts [strains less than a few percent (Biot 1973)] with a linear relation between effective stress and strain. In other words, strain is assumed to be fully recoverable. Furthermore, it is appropriate for timescales shorter than would be expected by crystal deformation due to dislocation or diffusion creep. Any poroviscous or poroplastic effects due to rearrangements of crystals on short timescales are neglected, under the assumption that the simulated porosity changes are small enough to allow this approximation (Marchal *et al.* 2013), even if they were to occur at timescales that are comparable to poroelastic deformation (Marchal *et al.* 2013). Including such processes would require adjusting the stress balance beyond Darcy's law.

The relative importance of poroelastic, poroviscoelastic, or poroplastic behaviour will likely depend on how coherent the mush framework is. Sintering of crystals, as suggested by Holness (2018), may favour a more coherent mush skeleton, which would favour poroelastic melt extraction, whereas less coherent frameworks may allow for poroviscous or poroplastic deformation through crystal rearrangement. These are all possibilities that could be investigated in subsequent work, assuming there are sufficient constraints on constitutive relations. We note neither foliation nor lineation textures are present in the enclaves at Cordón Caulle, which indicates a lack of evidence for significant crystal rearrangement due to settling or compaction (Winslow *et al.* 2022). We also note microtextures that indicate recrystallization or diffusion/dislocation creep (viscous deformation of the crystals) are often not observed in magmatic systems (Holness 2018).

The sequence of events for the model is as follows (Fig. 3). An eruption occurs over some time and removes a prescribed amount of material from the rhyolite layer. The rhyolite is assumed to have a sill-like geometry and surrounded by elastically deformable rock. Therefore, a change in volume of the sill, either due to magma eruptive withdrawal, expansion/contraction of the underlying mush, and/or melt addition from the mush, results in a change in pressure of the magma within the sill. Because the sill is assumed to be in direct contact with the underlying mush the pressure of the interstitial melt at the top of the mush must be equal to that of the overlying rhyolite. Thus, the rhyolite sill acts as a time-dependent pressure boundary condition for the underlying mush. A decrease in this pressure results in pressure gradients that induce upward flow of interstitial melt within the mush and from the mush into the overlying rhyolite.

Our model calculates how the melt pressure within the mush evolves over time and how melt flows from mush into the overlying rhyolite, as well as the resultant change in pressure of the rhyolite as it is being recharged from the mush.

## 4 THE MATHEMATICAL MODEL

### 4.1 System dimensionality

Although deformation patterns at Cordón Caulle allow for the possibility of multiple and somewhat interconnected magma bodies (Jay *et al.* 2014), co- and post-eruptive deformation can be reconciled with a sill-like magma body (Delgado *et al.* 2016; Delgado 2021). Based on these results, we approximate the rhyolite as an idealized rectangular sill of uniform thickness and laterally invariant magma pressure. We further assume the underlying crystal mush is contiguous with the rhyolite sill, of the same lateral dimensions, and with laterally invariant properties, including the pressure of the interstitial melt.

Our assumptions allow us to approximate the mush-rhyolite system as 1-D. Although this is a simplification, there are insufficient observational constraints to construct a geometrically more complex model. Furthermore, the 1-D approximation enables us to focus on the key elements for our assessment of whether the post-eruptive inflation at Cordón Caulle could be due to melt segregation from an underlying crystal mush. As already discussed, the assumption of no magma recharge into the mush, that is a no-flow boundary at the base of the mush, is also a simplification which could be eschewed in future investigations.

### 4.2 Magma mush

Modelling the poroelastic mush encompasses the elastic deformation of the crystal matrix and the flow of interstitial melt, both in response to a change in pressure of the overlying crystal-poor rhyolite. Interstitial melt flow results in the diffusion of pore pressure, whereas the crystal matrix responds elastically to any pressure changes. The diffusion of pore pressure constitutes the porous part of the poroelastic behaviour of the crystal-rich magma mush. The elastic part is encapsulated by the uniaxial specific storage coefficient,  $S_s$ , the volume of melt released from a volume of mush per unit change in pressure, assuming a constant vertical stress and negligible horizontal strain (see Appendices A and B for detailed derivations). It encapsulates the compressibility of both the crystal matrix and the interstitial fluid, which is mostly rhyolitic melt, but based on evidence from the mafic enclaves also contains small bubbles of exsolved volatiles (Winslow *et al.* 2022). We therefore use the melt-bubble mixture properties throughout our analysis.

Melt flow within the crystal-rich mush follows Darcy's law

$$q = -\frac{k}{\eta} \frac{\partial p}{\partial z} = -c \frac{\partial \zeta}{\partial z} = -\frac{c}{\rho_0} \frac{\partial m}{\partial z}, \quad (1)$$

where  $q$  is the volumetric flux of interstitial melt,  $p$  is the excess (non-hydrostatic) pressure of the interstitial melt,  $\eta$  is the melt viscosity,  $k$  is the permeability of the mush,  $c = k/\eta S_s$  is the effective diffusivity,  $\zeta$  is the volumetric change in the increment of interstitial melt content and  $m$  is the corresponding mass change (Biot 1956; Biot & Willis 1957; Wang 2000). Furthermore,  $\rho_0$  is the interstitial melt density in the reference state (Rice & Cleary 1976), which for our purposes will be the initial state of the model. Pore pressure and interstitial melt content are related through  $\partial \zeta / \partial z = S_s \partial p / \partial z$ ,

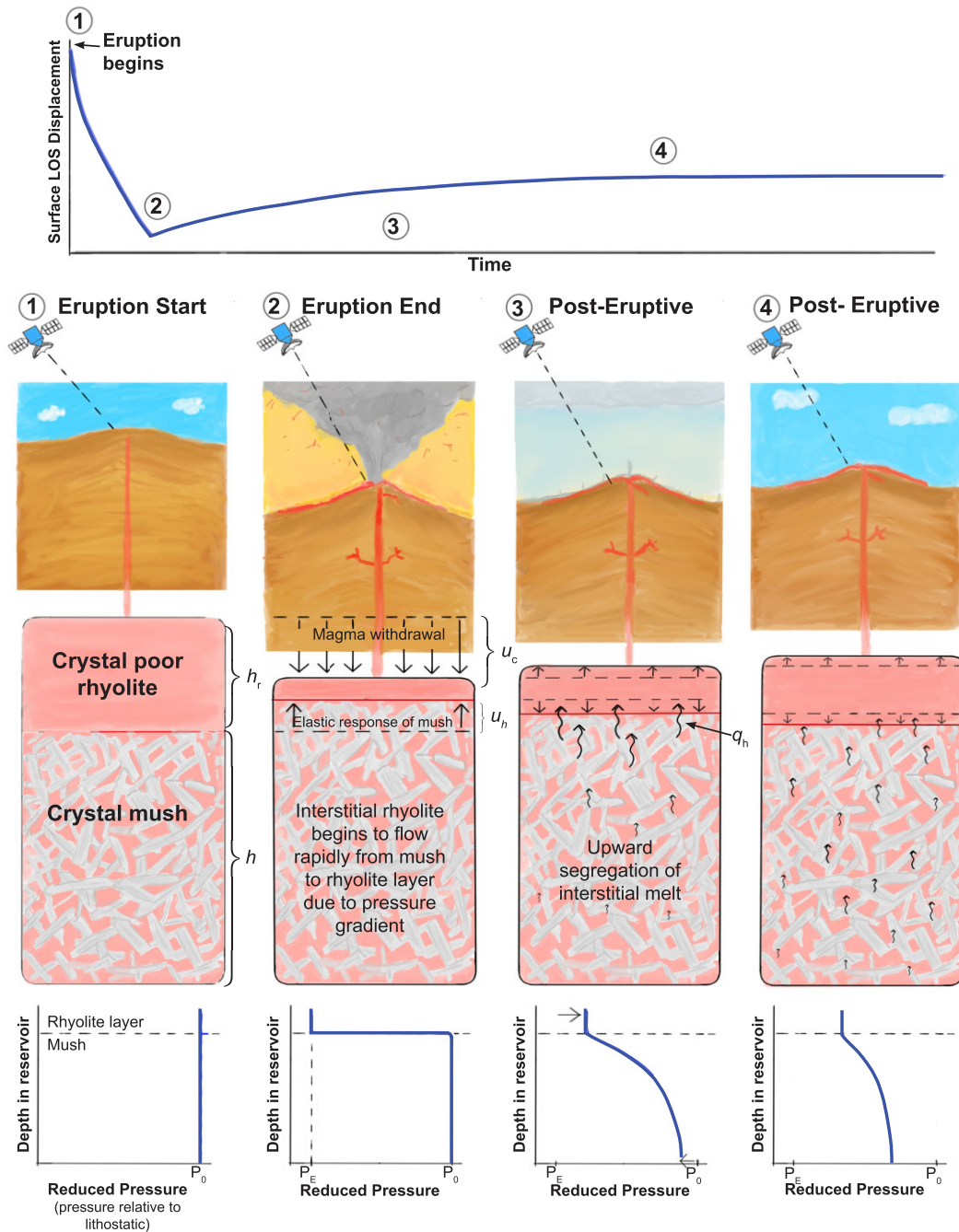


**Figure 3.** Conceptual model for the envisioned poroelastic reservoir. The schematic graph at the top shows a theoretical LOS displacement time-series associated with eruptive deflation and subsequent inflation due to melt segregation from the underlying crystal mush. The circled numbers correspond to each of the four schematic diagrams below. #1 corresponds to the assumed uniform state of the magma reservoir just as the eruption begins. #2 depicts the co-eruptive magma withdrawal and deflation and elastic expansion of the mush due to the reduction in vertical stress. #3 shows the re-inflation of the overlying rhyolite due to upward flow of interstitial melt and associated elastic contraction of the mush as pressure diffusion into the mush causes porous flow. #4 illustrates how the pressure gradient continues to evolve, producing deeper melt flow and a decreasing melt flux out of the mush. The schematic graphs at the bottom show the corresponding reduced (non-hydrostatic) pressure within the reservoir.

assuming no body forces, and  $\zeta = m/\rho_0$ . By virtue of conservation of mass, the flux,  $q$ , produces a time rate of change in  $\zeta$  (Biot 1956; Rice & Cleary 1976; Wang 2000), given by

$$\frac{\partial \zeta}{\partial t} = -\frac{\partial q}{\partial z}, \quad \text{or equivalently} \quad \frac{\partial m}{\partial t} = c \frac{\partial^2 m}{\partial z^2}, \quad (2)$$

where the effective diffusivity,  $c$ , is assumed constant.

There are multiple ways to set up eqs (1) and (2) to model deformation in a magma mush. For instance, one could pose the equations in terms of mush pore pressure. An advantage of using pore pressure is the intuitive approach one can take to deriving boundary conditions. However, when pore pressure is used, eq. (2) becomes inhomogeneous due to changes in the mean stress with time [see Roeloffs (1996) and discussion surrounding eq. 4.63 in Wang

(2000)]. This adds an extra term that must be solved at every time step in the model. Using  $m$  relegates this behaviour to the boundary condition and makes the partial differential equation homogeneous. This methodology is also consistent with recent work that uses a linear poroelastic model to model deformation and magma transport within a magma mush (Liao *et al.* 2018). We therefore pose the problem in terms of  $m$ . In the following sections, we will derive the boundary conditions in terms of pressure and how to cast those conditions in terms of  $m$ .

### 4.3 Crystal-poor rhyolite

#### 4.3.1 Surface deformation

The sill-like geometry that allows for the 1-D geometry of our model equations results in a model where pressure changes within the rhyolite are a linear function of the assumed reservoir volume. Moreover, surface uplift is calculated using a linear transfer function that is dependent on pressure. Magma withdrawal or inflow from the underlying mush will result in a mass change,  $\Delta M$ , of this rhyolite and a subsequent volume change,  $\Delta V$ , due to the displacement of the surrounding/overlying country rock, which we assume to deform elastically. Approximating the opening/closing displacement as laterally uniform for the entire sill, we reduce  $\Delta V$  to a change in thickness defined as  $u_c - u_h = \Delta V/A$ , where  $A$  is the areal extent of the sill,  $u_c$  is the displacement of the upper rock-rhyolite interface and  $u_h$  is the vertical displacement of the top of the mush. Using standard formulations for displacement and pressure changes (Okada 1992), we define two transfer functions

$$\Psi_u = \frac{u_c}{P} \quad \text{and} \quad \Psi_w = \frac{w}{u_c}. \quad (3)$$

$P$  is the reduced pressure of the rhyolite, defined as  $P = \mathcal{P}(t) - P_{\text{ref}}$ .  $P_{\text{ref}}$  is the reference pressure of the system prior to eruption and assumed lithostatic and  $\mathcal{P}$  is the total pressure. We assume that  $\mathcal{P}(t=0) = P_{\text{ref}}$ . The  $\Psi_u$  transfer function allows us to calculate displacements of the host rock-rhyolite interface,  $u_c$ , due to a change in reduced pressure,  $P$ , in the rhyolite. This displacement is then propagated to the surface according to  $\Psi_w$ , which gives the ratio of surface displacement to  $u_c$ . Furthermore,  $w$  is the maximum vertical surface displacement (Fig. 3) to be compared to the LOS proxy data. We note  $w$  will always be less than  $u_c$  (Okada 1992), since the vertical displacement from  $u_c$  will translate to both vertical displacement at the surface as well as some lateral deformation.

To calculate the transfer functions, we use a MATLAB<sup>®</sup> wrapper from Toda *et al.* (2011) of the original FORTRAN code that solves the equations presented in Okada (1992). The sill model returns the displacement and its derivative at a point in space given a sill geometry (cross sectional area, depth, aspect ratio and dip), a shear modulus of the host rock, a Poisson's ratio, and a sill opening amount. The model then calculates the stresses and displacements at the point specified. We use this sill model to iteratively calculate the pressures that produces a specific change in sill thickness and associated maximum surface displacement. We then determine the linear relation between pressure and sill opening, which we define as  $\Psi_u$ . The term  $\Psi_w$ , in turn, is the linear relation between the sill opening and the maximum surface displacement. The value of  $\Psi_u$  multiplied by the host rock's shear modulus is a constant, and  $\Psi_w$  is constant for a given sill geometry.

#### 4.3.2 Pressure of the crystal-poor rhyolite

The change in mass of the rhyolite layer,  $\Delta M$ , leads to a Dirichlet pressure boundary condition on the mush. That change can be expressed in two ways: through the rhyolite fluxes in and out of the layer, and by the changes in volume and density of the melt. In terms of fluxes,

$$\frac{dM}{dt} = \frac{dM_{\text{mush}}}{dt} - \frac{dM_{\text{E}}}{dt} = A\rho_0 q_h - Q, \quad (4)$$

with  $M_{\text{mush}}$  being the rhyolite mass leaked from the mush and  $M_{\text{E}}$  being that erupted from the rhyolite layer. This difference in mass fluxes is then expressed in terms of  $Q$ , the rate of mass erupted (e.g. Fig. 4) and  $q_h$ , the Darcy flux at the top of the mush from eq. (1). Details of its derivation can be found in Appendix B2.2.

Given that  $\Delta M = \Delta(\rho V)$ , the time rate of change in  $\Delta M$  can also be expressed as

$$\frac{dM}{dt} = \rho_0 \frac{dV}{dt} + V_0 \frac{d\rho}{dt} = A\rho_0 \frac{d(u_c - u_h)}{dt} + Ah_r \rho_0 \beta_r \frac{dP}{dt}, \quad (5)$$

where following Rice & Cleary (1976), we have linearized  $\rho$  and  $V$ . Here,  $h_r$  is the initial thickness of the rhyolite layer. Throughout, the subscript 'r' denotes properties of the rhyolite layer. Furthermore,

$$\beta_r = \frac{1}{\rho} \frac{\partial \rho}{\partial P} \quad (6)$$

is the compressibility of the rhyolite melt plus volatile bubbles mixture, which we assume constant (e.g. Rice & Cleary 1976; Anderson & Segall 2011). We define the inverse bulk modulus of the interstitial melt-bubble mixture,  $1/K_r$ , by assuming an ideal gas phase for the supercritical fluid mixture inside bubbles

$$\beta_r = \frac{1}{K_r} = \frac{\phi_g}{P_{\text{ref}}} + \frac{1 - \phi_g}{K_{\text{melt}}}. \quad (7)$$

Here,  $\phi_g$  is the volume fraction of bubbles in the mixture. One can use an equation of state other than an ideal gas, but considering the uncertainties in the model parameters which are discussed in Section 5 and Appendix C1, we assume ideal behaviour. A final form of eq. (5) that includes an expression for  $du_c/dt$  from eq. (3) is

$$\frac{dM}{dt} = A\rho_0 \left[ \left( \Psi_u + \frac{h_r}{K_r} \right) \frac{dP}{dt} - \frac{du_h}{dt} \right]. \quad (8)$$

Equating the two expressions for the time rate of change in mass of the crystal-poor rhyolite (eqs 4 and 8) gives

$$\frac{dP}{dt} = \left[ \Psi_u + \frac{h_r}{K_r} \right]^{-1} \left[ q_h(t) - \frac{Q(t)}{\rho_0 A} + \frac{du_h}{dt} \right]. \quad (9)$$

The time rate of change for the displacement of the top of the mush,  $du_h/dt = du/dt|_{z=h}$ , implicitly depends on  $P$ . An expression for it is derived in Appendix B2.3, and is

$$\frac{du_h}{dt} = -\gamma q_h - \frac{h}{\tilde{K}_v} \frac{dP}{dt}. \quad (10)$$

Combining eq. (10) with eq. (9) gives

$$\frac{dP}{dt} = \frac{1}{\Omega} [(1 - \gamma) q_h(t) - Q(t)], \quad (11)$$

where

$$\Omega = h_r \beta_{\text{eff}} = h_r \left( \frac{1}{K_r} + \frac{\Psi_u}{h_r} + \frac{h}{h_r \tilde{K}_v} \right) \quad (12)$$

is the scaling between change in length and change in pressure of the crystal-poor rhyolite magma,  $\beta_{\text{eff}}$  is the *effective* compressibility

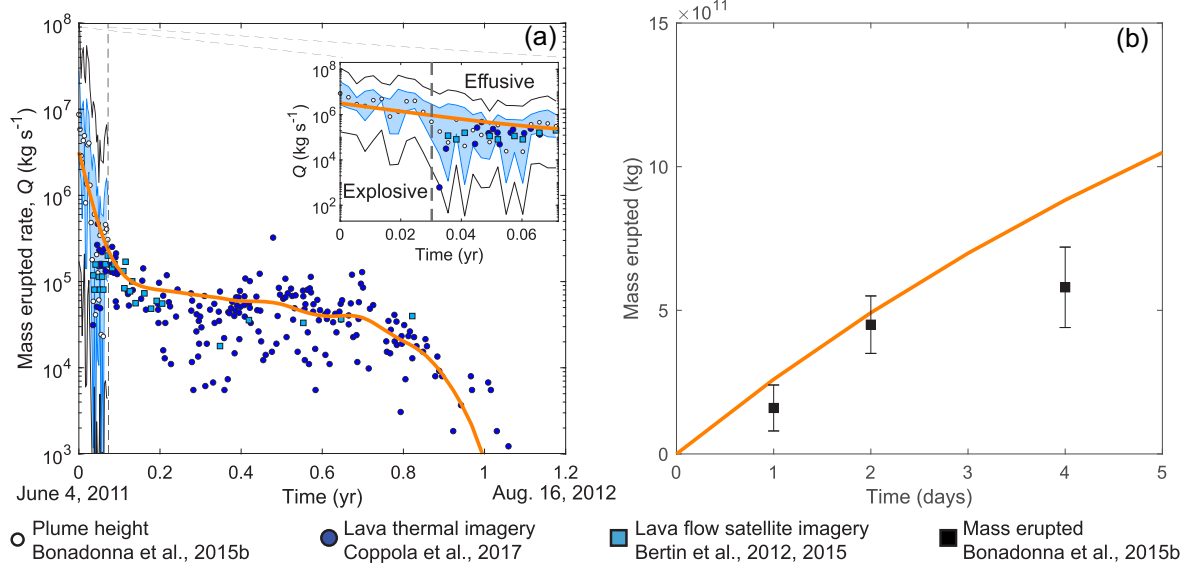


**Figure 4.** Eruption rate estimates and corresponding cubic spline. (a) Estimates of mass eruption rates as a function of time obtained from plume height data [white circles; Bonadonna *et al.* (2015b)], satellite imagery of the lava flow [blue squares; Bertin *et al.* (2012, 2015)], and lava thermal data [blue circles; Coppola *et al.* (2017)]. Lava began extruding on 15 June 2011. Estimates up to this point are solely from plume height. The blue band indicates uncertainty surrounding plume height and atmospheric conditions. The white band includes all other sources of uncertainty. Inset gives the first 26 d of the eruption when plume height proxies for mass discharge rate were estimated. (b) Mass erupted over the first 4 d as estimated by Bonadonna *et al.* (2015b). Orange line in (a) and (b) is the fit to the eruption rate used in the model and denoted as  $Q$ .

of the crystal-poor rhyolite magma, and

$$Q(t) = \frac{1}{\rho_0 A} Q(t) \quad (13)$$

is the volumetric magma eruption rate.

Each term in  $\beta_{\text{eff}}$  (eq. 12) corresponds with a compressibility for different components of the crystal-poor rhyolite magma. The first term,  $1/K_r$ , is the compressibility of the mixture of the rhyolite melt and volatile bubbles,  $\Psi_u/h_r$  represents how compressible the host rock is, and  $h/h_r \tilde{K}_v$  defines the strength of the top of the mush. Interestingly, this last term modulates the undrained compressibility of the mush by the ratio of the mush size to the rhyolite size. Relatively larger mushes will impact the effective compressibility through this term compared to larger rhyolite layers. The term  $\Omega$  then scales this effective compressibility to a change in length given a change in pressure. The three terms  $1/K_r$ ,  $\Psi_u/h_r$  and  $1/\tilde{K}_v$  are each a component of the rhyolite layer's strain due to compressibility, so that the change in length of the rhyolite is the sum  $h_r/K_r + \Psi_u + h/\tilde{K}_v$ .

## 4.4 Initial and boundary conditions

### 4.4.1 Initial conditions

We assume that our simulations start from a static initial state with no flow of interstitial melt within the mush. Thus, at  $t = 0$  we assume  $m(z) = 0$  and  $\partial p/\partial t = 0$ . This is likely a simplification, given that prior to the eruption there was inflationary deformation, albeit at a significantly lower rate than deformation during and immediately after the eruption (Delgado 2021). Using a non-stationary initial state would require a different and more complicated set of assumptions. We therefore choose the simpler approach of assuming a static

initial state. Future work, however, could attempt to assess the effect of a non-stationary initial state.

### 4.4.2 The mass eruption rate

Eruption rates for the Plinian to subplinian phase of the eruption have been estimated on the basis of plume height (Fig. 4) to range from approximately  $3 \times 10^6$  to  $3 \times 10^7$   $\text{kg s}^{-1}$  initially and subsequently decreased to  $10^5$  to  $10^6$   $\text{kg s}^{-1}$  (Bonadonna *et al.* 2015b). The subsequent effusive phase, which included vigorous ash venting (Schipper *et al.* 2013; Crozier *et al.* 2022) and formation of a lava flow, had initial effusion rates of approximately  $3 \times 10^5$   $\text{kg s}^{-1}$  that decreased over time to approximately  $3 \times 10^4$   $\text{kg s}^{-1}$ . These rates are estimated from satellite thermal data (Coppola *et al.* 2017) and from volume changes of the lava flow that were estimated from satellite images taken at different times throughout the eruption (Bertin *et al.* 2012, 2015).

A function for the mass eruption rate  $Q(t)$  is required for the calculation of  $P$  (eq. 11). We obtain  $Q(t)$  from a smoothing cubic spline interpolation of the aforementioned discharge rate estimates shown in Fig. 4. Calculation of the smoothing spline was done using the MATLAB<sup>®</sup> function `csaps`, which minimizes the error between  $Q(t)$  and the discharge rate estimates under a smoothness constraint,  $\theta$ . The data were weighted to obtain a monotonically decreasing function of  $Q$  with respect to time. The value of  $Q(t = 0)$  was chosen such that the time integral of  $Q$  falls within a reasonable range of estimates for the total erupted mass during the first few days of the eruption (Bonadonna *et al.* 2015a; Pistolesi *et al.* 2015), which are shown in Fig. 4(b). The resulting function  $Q(t)$  and its time integral are also shown in Figs 4(a) and (b), respectively. It is based on  $Q(t = 0) = 3.2 \times 10^6$   $\text{kg s}^{-1}$  and a smoothness parameter of  $\theta = 1 \times 10^{-19}$ .

#### 4.4.3 Boundary conditions for the mush

As already discussed, at the bottom of the crystal mush, we assume a no-flow (Neumann) boundary condition

$$\frac{dm}{dz} = 0 \quad \text{at } z = 0. \quad (14)$$

In reality a shallow crustal magmatic system may be contiguous at depth with a more extensive crustal magma transport and storage system. If so, one question would be to what extent permeability and other properties vary with depth. Moreover, it is hard to imagine that the mush is not an open system in the sense that there would not be a deeper magma supply, at least on longer timescales (e.g. Cashman *et al.* 2017; Hildreth 2021). Because our objective is to assess to what extent the observed inflationary deformation since the eruption can be explained by melt percolation from a crystal mush, as opposed to recharge, we assume a no-flow boundary at the bottom of the mush. In other words, some extent of magma recharge from below can always be invoked to explain volcano inflation, here we wish to assess the viability of the *closed-system* response on the decadal timescale of a potential mush beneath Cordón Caulle. It should be noted that the no-flow assumption is also consistent with the aforementioned static initial state approximation, allowing us to isolate the response of the magma mush to the eruption.

At the top of the crystal mush ( $z = h$ ), that is at the interface between the mush and overlying crystal-poor rhyolite melt, the pressure of the interstitial rhyolite melt within the mush and within the crystal-poor rhyolite must be continuous. We thus impose a time-dependent Dirichlet boundary condition that represents the reduced pressure,  $P$ , of the crystal-poor rhyolite melt in contact with the top of the mush. The value of  $P$  is calculated using eq. (11), with the added complication that this pressure boundary condition must be expressed in terms of  $m$ , for use with eq. (2). Therefore,  $P$  must be expressed in terms of  $m$ . This relation is given by (see Appendix B2.3)

$$m_h(t) = \rho_0 S_s (1 - \gamma) P(t). \quad (15)$$

where  $m_h = m(z = h)$ . Combined with eq. (11), eq. (15) is the boundary condition for the top of the mush, and the entire problem to be solved is given by eqs (2), (11), (14) and (15).

#### 4.4.4 Surface deformation

To predict surface displacement,  $w$ , we incorporate the transfer functions (see Section 4.3.1 for a more detailed discussion of how the transfer functions are calculated) as calculated by Okada (1992) in eq. (3) and write

$$w(t) = \Psi_w \Psi_u P(t). \quad (16)$$

The term  $w$  is the predicted maximum vertical surface displacement, which occurs directly over the centre of the sill. The LOS displacement may be different from this value, depending on the angle of incidence, the direction of deformation, and where on the volcano it is measured. Our LOS proxy data (Fig. 1b) has some variability in incidence angle and location (Delgado 2021). We also do not know the direction (compared to vertical) of maximum deformation for these LOS proxies. This would require re-analysing the descending and ascending interferograms that led to the LOS points to retrieve the vertical and horizontal components of the LOS displacement. Alternatively, one could assume a pseudo-vertical displacement by dividing the LOS by the cosine of the incidence angle (e.g. Delgado

*et al.* 2016), although this assumes all displacement to be in the vertical direction, which would likely overestimate the actual vertical displacement. For simplicity, we therefore compare  $w$  to the LOS displacement. Also, our objective is to assess the feasibility of melt segregation from a mush causing uplift. Comparing  $w$  to the LOS displacement directly allows us to test this feasibility.

### 4.5 Numerical method for the time-dependent problem

Eq. (2), together with boundary conditions given by eqs (11) and (14), as well as eq. (15), are solved by the Method of Lines (e.g. Fletcher 1998) using the MATLAB<sup>®</sup> solver `ode15s`. The main result of these simulations is the prediction of  $m(t)$ , which allows the estimation of the surface uplift,  $w$ , using the relations from eqs (15) and (16). The values of  $w(t)$  can be compared against the LOS displacements shown in Fig. 1(c).

## 5 PARAMETER ESTIMATION

### 5.1 Objective

The model defined in the previous section, comprised of eqs (2), (11), (14), (15) and (16), depends on six poroelastic parameters:  $K_s$ ,  $G$ ,  $\phi_0$ ,  $\alpha$ ,  $k$  and  $S_s$ , plus melt viscosity  $\eta$ . The remaining poroelastic parameters are dependent on these parameters as summarized in Table 1. Parameters that do not directly affect the mechanics of the poroelastic mush, but nevertheless affect the simulation results, are summarized in the lower part of Table 1 and include the mush thickness,  $h$ , the thickness of the rhyolite,  $h_r$ , the mush depth,  $d$ , the areal extent,  $A$ , of the Cordón Caulle magmatic system and the shear modulus of the host rock,  $G_c$ . Most of these parameters can be constrained based on prior information. Only three parameters,  $S_s$ ,  $h$  and  $h_r$ , are truly unknown and will be estimated through model simulation.

To achieve the parameter estimation, we solve the aforementioned equations in order to predict vertical surface displacements that we match to the LOS displacements (Fig. 1c) as closely as possible. As discussed previously, this approach neglects the fact that the LOS displacements are not exactly equal to vertical surface uplift. Both the poroelastic response of the mush and the eruption rate  $Q$  jointly result in surface deformation. Because the eruption lasted for almost one year, the response of the mush to eruptive magma withdrawal from the overlying rhyolite already begins during the eruption. It is therefore difficult to limit our simulations solely to the time after the eruption. Furthermore, parameters that do not govern the response of the mush nevertheless affect model predictions, in particular the magnitude of predicted surface deformation, both during deflation and inflation. Therefore, we simulate the entire time period, starting from the beginning of the eruption until early 2020.

To quantify the match between simulated surface deformation and the LOS displacements we define a model misfit,  $\chi$ , which is the root mean square error between the simulated surface deformation and the LOS displacements. It is given by

$$\chi \equiv \text{RMSE} = \sqrt{\frac{1}{n} \sum_{j=1}^n \mathcal{W}_j (w_j - \text{LOS}_j)^2}. \quad (17)$$

Here,  $\text{LOS}_j$  corresponds with the  $j$ th LOS displacement value from Delgado (2021) and  $w_j$  is the corresponding simulated (predicted) maximum vertical displacement based on the assumed sill geometry (discussed in Section C1.8 and shown in Fig. 1b). The weights  $\mathcal{W}_j$

**Table 1.** Model parameters related to the poroelastic mechanics of the crystal mush and their interdependencies as well as other parameters that define the geometry of the reservoir and the rock properties. See Appendix C1 for explanations of the parameter ranges and Section 4.3.1 for an explanation of how the transfer functions are calculated.

Symbol	Units	Definition	Value
Poroelastic parameters			
$\alpha$	(-)	Biot–Willis coefficient	0.5–0.9
$\phi_0$	(-)	Initial mush porosity	0.36
$K_s$	(Pa)	Bulk modulus of the crystals matrix	$87.6 \times 10^9$
$G$	(Pa)	Shear modulus of mush	$11.2 \times 10^9$
$\eta$	(Pa s)	Melt viscosity	3300
$k$	(m <sup>2</sup> )	Mush permeability	$1.7 \times 10^{-9}$ – $6.7 \times 10^{-9}$
$a$	(m)	Grain size	0.001–0.002
$S_s$	(Pa <sup>-1</sup> )	Uniaxial specific storage coefficient	$\alpha^2 \tilde{K}_v / (K_v \tilde{K}_v - K_v^2)$ , Estimated
$K$	(Pa)	Drained bulk modulus of mush	$(1 - \alpha)K_s$
$K_r$	(Pa)	Rhyolite-bubble mixture bulk modulus	$\phi_0 / [S_s - (\alpha - \phi_0)K_s - \alpha^2/K_v]$
$\tilde{K}$	(Pa)	Undrained bulk modulus of mush	$K + \alpha^2 K_s K_r / [\phi_0 K_s + (\alpha - \phi_0)K_r]$
$K_v$	(Pa)	Vertical drained bulk modulus of mush	$K + 4/3G$
$\tilde{K}_v$	(Pa)	Vertical undrained bulk modulus	$\tilde{K} + 4/3G$
$\gamma$	(-)	Loading efficiency	$\alpha / (K_v S_s)$ or $(1 - K_v / \tilde{K}_v) / \alpha$
$c$	(m <sup>2</sup> s <sup>-1</sup> )	Pressure diffusivity of the mush	$k / (\eta S_s)$
Other parameters			
$h$	(m)	Initial mush layer thickness	Estimated
$h_r$	(m)	Initial rhyolite layer thickness	Estimated
$A$	(m <sup>2</sup> )	Magma chamber areal footprint	$60 \times 10^6$ m <sup>2</sup>
$h_r A$	(km <sup>3</sup> )	Rhyolite volume	>1.65 km <sup>3</sup>
$d$	(m)	Magma chamber depth	6000 m
$G_c$	(Pa)	Host rock shear modulus	$1$ – $35 \times 10^9$ Pa
$\Psi_u$	(m Pa <sup>-1</sup> )	Transfer function for pressure to rock displacement	$4621.7/G_c$
$\Psi_w$	(-)	Transfer function for rock displacement to surface displacement	0.3324
$\Omega$	(m Pa <sup>-1</sup> )	Scaled compressibility of the magma chamber	$h_r / K_r + \Psi_u + h / \tilde{K}_v$

have a value of one, except  $\mathcal{W}_1$  and  $\mathcal{W}_2$ , which are zero because of the large rate of change in LOS during the first few hours of the eruption as well as the large uncertainty in eruption rates during that time (Fig. 4). Our weighting of the LOS data ensures that low values of  $\chi$  meet our objective of quantifying the misfit to the inflationary part of the LOS data.

Although we are searching for the best fit to the LOS displacements, we wish to reiterate the inherent imperfections in this data. The LOS proxies are a compilation of varying orbital angles and a moving locus of maximum deformation, particularly during the eruption, which have been spliced together to provide a continuous signal. As such, the exact misfit value should be viewed with these caveats in mind. We also note that our goal is not to match the uplift data any better than was already done using elastic and viscoelastic models (Delgado *et al.* 2016, 2018). We only wish to illustrate what is necessary for a mush to produce all of the measured uplift.

## 5.2 Parameter estimation

Because the dimensionality of parameter space makes a grid search prohibitive, we conducted an exploratory random sampling (e.g. Kochenderfer & Wheeler 2019) of all parameters within some pre-defined range. The exact parameters values and ranges as well as dependencies are summarized in Table 1. Explanations of how we came to these ranges and values are given in Appendix C1. *Random sampling* herein refers to using MATLAB<sup>®</sup>'s pseudo-random number generator to produce a set of values for each parameter

within the range we wish to cover. The purpose of this random sampling was to explore parameter space with respect to relationships between parameters. Our results of this random sampling are presented in Appendix C1.12.

We found that for any combination of parameters there is a unique value of both  $S_s$  and  $\eta/k$  for which the misfit  $\chi$  is the smallest. This is denoted as  $\chi_{\text{opt}}$ . For some combinations of parameters the smallest value of  $\chi$  found within  $S_s$ – $\eta/k$  space corresponds to the minimum in  $\chi$  that can be achieved for any combination of parameters. We denote this value as  $\chi_{\text{min}}$ . We emphasize that it is not a unique minimum, because more than one combination of parameters can produce this minimum value of  $\chi$ . We seek parameter combination that result in  $\chi_{\text{min}}$ .

The parameter combination  $\mathcal{A}$  ( $\alpha = 0.7$ ,  $K_s = 88$  GPa,  $G = 15$  GPa and  $\phi_0 = 0.42$ ) gives the minimum misfit value of  $\chi_{\text{opt}} = \chi_{\text{min}} = 3.75$  cm (Fig. 5a). In contrast, the combination  $\mathcal{F}$ , comprising a higher value of  $\alpha$ , a lower value of  $\phi_0$  and a lower value of  $G$ , gives a corresponding smallest misfit value of  $\chi_{\text{opt}} > \chi_{\text{min}}$  (Fig. 5b). The modelled solution corresponding to  $\mathcal{A}$  provides a distinctly better fit to the LOS time-series than that corresponding to  $\mathcal{F}$  (Fig. 5c).

Four other simulations, labelled as  $\mathcal{B}$ ,  $\mathcal{C}$ ,  $\mathcal{D}$  and  $\mathcal{E}$  in Fig. 5(d), illustrate how changes in parameters affect the misfit. Parameters can affect the rate at which the poroelastic response occurs, the magnitude of the response, or both, where the response magnitude is the final LOS displacement amount. The rate at which the mush responds to pressure changes in the rhyolite is dependent on

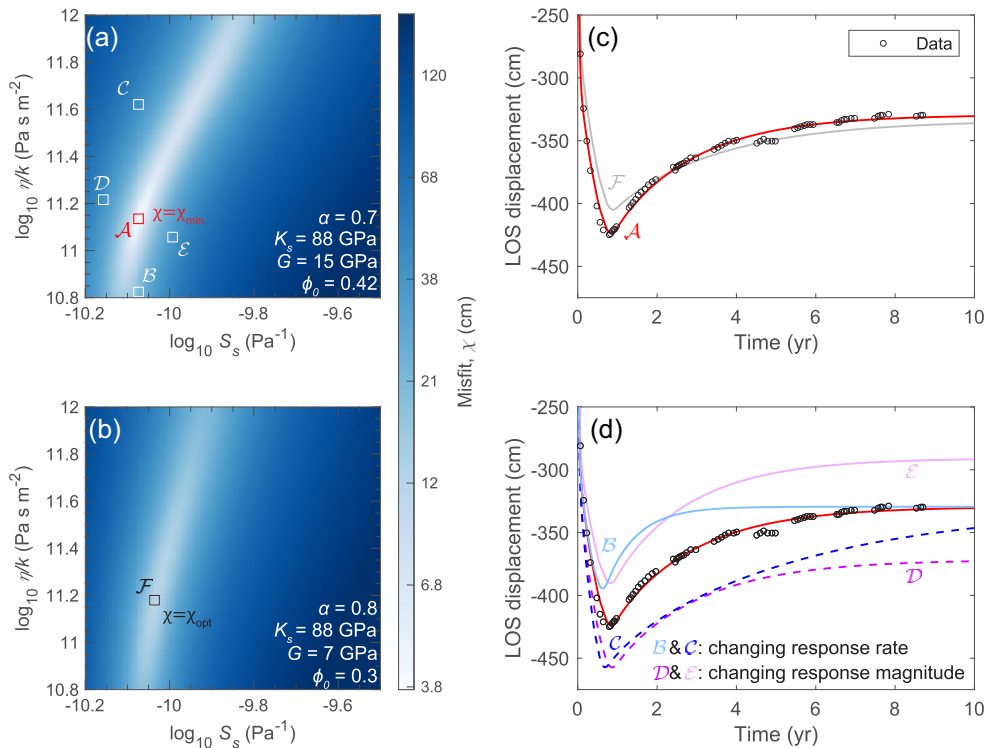


**Figure 5.** Correspondence between misfit and LOS displacement time-series. (a) Misfit as a function of  $S_s$  and  $\eta/k$  for a 100 by 100 grid. Darker blue indicates larger misfit. Parameter choices are  $\alpha = 0.7$ ,  $K_s = 88$  GPa,  $G = 15$  GPa and  $\phi_0 = 0.42$  (identical to the reference case shown in Fig. C1). (b) Same as (a), but for values of  $\alpha = 0.8$ ,  $G = 7$  GPa and  $\phi_0 = 0.3$ . In this case the smallest misfit, labelled as  $\mathcal{F}$  does not correspond to  $\chi_{\min}$ . In other words, at  $\mathcal{F}$  the misfit  $\chi_{\text{opt}}$  is greater than  $\chi_{\min}$ . (c) This graph illustrates the match between the calculated vertical displacement and the LOS displacements for two cases: One corresponding to a misfit of  $\chi_{\min}$  at the point labelled  $\mathcal{A}$  in (a) and the other corresponding  $\chi_{\text{opt}} > \chi_{\min}$  at the point labelled  $\mathcal{F}$  in (b). In the case of  $\chi_{\min}$  to match between predicted uplift and LOS displacements is close, whereas for the case  $\mathcal{F}$  in (b) it is clearly not as close a match. It should be noted that all cases corresponding to  $\chi_{\min}$  are indistinguishable and represent the best fit to the LOS time-series attainable by our model. (d) This graph illustrates how changes in  $S_s$  and  $\eta/k$  affect the match of modelled uplift to the LOS time-series.

the characteristic pore-pressure diffusion time of the mush,  $\tau = h^2 S_s \eta / k$ . Because  $S_s$  and  $h$  also affect the response magnitude in simulated uplift, a change in  $\eta/k$  will influence the rate of uplift. For instance, higher permeability enables more rapid melt segregation, facilitating an accelerated poroelastic recovery. The final amount of recovery remains unchanged, leading to the same final LOS displacement value as a lower permeability case. However, the extent of deflation will vary due to the faster recovery, which corresponds to increased melt segregation during the eruption and leads to less deflation. Varying any of the parameters  $A$ ,  $h_r$ ,  $G_c$ ,  $\Psi_u$  and  $\Psi_w$  will change the magnitude of simulated uplift only, shifting the entire curve vertically. Here it should be kept in mind that the simulated uplift is also dependent on  $\mathcal{Q}$ , the mass eruption rate, which we have not varied between simulations from what is shown in Fig. 4.

The values of  $\chi_{\text{opt}}$ , which are obtained from a random sampling of all parameters with minimization over  $S_s$  and  $\eta/k$ , can be shown to have well defined functional dependencies (see Appendix C1.12). These functional dependencies are expressed in terms of three functions  $\Gamma_1$ ,  $\Gamma_2$  and  $\Gamma_3$  that encompass the three unknown parameters  $S_s$ ,  $h$  and  $h_r$  (C2). It is therefore possible to leverage these functional relations to find which parameter combinations yield the minimum misfit of  $\chi_{\min} = 3.75$  cm. Specifically, for a given set of *a priori* parameters that are either constrained to a specific value or to

within a defined range (see Table 1), we can find those combinations of  $S_s$ ,  $h$  and  $h_r$  that have  $\chi$  as the smallest misfit in  $S_s$ - $\eta/k$  space.

## 6 DISCUSSION OF RESULTS

### 6.1 Mush properties

The best fits of model simulations to the LOS displacements, that is solutions corresponding to  $\chi_{\min}$ , provide estimates for the specific storage of the mush,  $S_s$ , the thickness of the mush,  $h$  and the thickness of the overlying crystal-poor rhyolite,  $h_r$ . As already discussed in the previous section, these estimates are based on prior constraints of other parameters, as summarized in Appendix C1 and in Table 1. Furthermore, it should be kept in mind that the LOS displacements provide a proxy for deflationary and inflationary deformation at Cordón Caulle, whereas the simulated time-series represents vertical displacements that are from a model that is based upon a number of simplifying assumptions. Thus, the results presented here should solely be viewed within the context of testing the the feasibility that inflationary deformation after the eruption could be due to melt segregation from a crystal mush. In other words, our parameter estimates provide an assessment of the extent to which the conditions required for the crystal mush hypothesis to hold are feasible.

Throughout, we assume a homogeneous mush with constant values for all parameters. In nature this seems unlikely. For example, a magma mush beneath Cordón Caulle could be stratified such that porosity, which affects  $k$ , or volatile bubbles within the interstitial melt, which affects  $S_s$ , could vary with depth (e.g. Bachmann & Bergantz 2004; Hildreth & Wilson 2007; Cashman *et al.* 2017; Sparks *et al.* 2019). If that were the case, then our model would be more representative of the shallower parts of a vertically more extensive mush system (e.g. Hildreth 2004; Hildreth & Wilson 2007; Cashman *et al.* 2017; Hildreth 2021).

We present our results in Fig. 6 as a function of mush permeability,  $k$ , which is treated as if it were an independent parameter, even though we have constraints on  $k$  that are based on the Cordón Caulle enclaves (see discussion in Appendix C1). The range is based on values that are consistent with permeabilities for partially crystallized rocks and other porous materials at similar porosities and grain sizes as the enclaves (Hersum *et al.* 2005). However, because it is well known that field-scale permeabilities can be considerably larger than permeabilities measured at the sample-scale (e.g. Clauser 1992; Schulze-Makuch *et al.* 1999), for example due to the presence of highly permeable pathways, we have extended the permeability range considered by an order of magnitude.

We estimate the specific storage of the mush,  $S_s$ , to fall within the range of about  $10^{-10}$  to  $10^{-9}$  Pa $^{-1}$  (Fig. 6a). The specific storage represents the amount of interstitial rhyolite released from the mush per unit volume of mush. It depends on the elastic deformability of the crystal matrix of the mush, as well as the compressibility of the pore fluid, in this case rhyolite melt with volatile bubbles. The value of  $S_s$  therefore is strongly dependent on the volume fraction of bubbles within the interstitial melt, as indicated by eqs (7) and (C3). It is commonly assumed that mush systems associated with evolved magmas contain exsolved volatiles (e.g. Wallace 2001; Shinohara 2008), due to crystallization-driven exsolution (*second boiling*) and/or the degassing of deeper recharge of magma. As discussed by Parmigiani *et al.* (2016), despite their buoyancy, bubbles can remain trapped within a mush due to capillary and viscous forces at values of  $\phi_g \leq 0.15$  (see discussion in Appendix C1). We therefore consider solutions of  $S_s \leq 4.3 \times 10^{-10}$  Pa $^{-1}$  as viable, as indicated in Fig. 6(a).

Within the observational constraints of enclave permeability and vesicularity, the observed uplift can be explained by melt segregation from a mush. Where these conditions are all met is indicated by the circle and arrow in Fig. 6. The permeability here is  $k \approx 6.7 \times 10^{-9}$  m $^2$ , and the corresponding specific storage is  $S_s \approx 4 \times 10^{-10}$  Pa $^{-1}$ , which corresponds to  $\phi_g \approx 0.15$ . Permeabilities of  $k < 6.7 \times 10^{-9}$  m $^2$ , which fall within the range of sample-scale estimates obtained from measured enclave porosities and crystal sizes. Because they require gas fractions of  $\phi_g > 0.15$  we consider them as unlikely. In contrast, the possibility that the effective permeability of the mush at the field-scale is somewhat larger than the sample-scale estimates would allow a larger volume of mush with values of  $S_s$  corresponding to gas fractions as low as a few percent.

The corresponding estimates for the crystal-poor rhyolite thickness (Fig. 6b) and underlying crystal mush (Fig. 6c) are  $h_r \approx 260$  m (volume of  $V_r \approx 15.6$  km $^3$ ) and  $h \approx 1$  km (volume of  $V \approx 60$  km $^3$ ), respectively. To put these values in perspective, the predicted crystal-poor rhyolite volume is ten-fold of what erupted in 2011–2012, implying that more than 14 km $^3$  of crystal-poor rhyolite could still remain beneath Cordón Caulle. The rhyolite predicted to be contained within the mush is slightly more than that. Approximately 25 per cent of the erupted volume would have been recharged by melt segregation from the mush, which equates to a

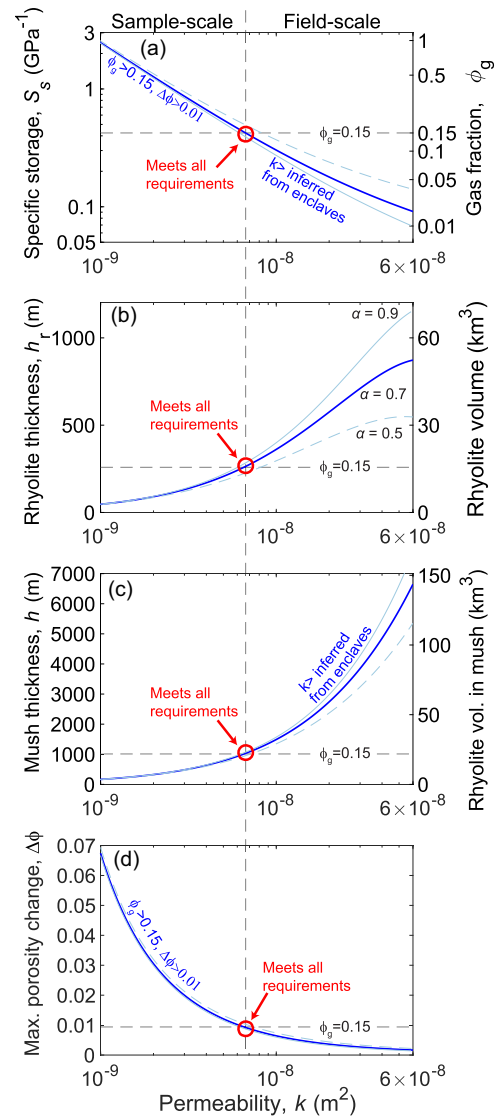


**Figure 6.** Estimates of the properties that would be required for a hypothetical crystal mush beneath Cordón Caulle, if the inflationary deformation after the 2011–2012 eruption were solely due to melt segregation from the mush recharging the rhyolite reservoir from which the 2011–2012 magma erupted. (a) The required specific storage,  $S_s$  and volume fraction of volatile bubbles,  $\phi_g$ , within the interstitial melt of the mush. (b) The required rhyolite thickness,  $h_r$ , and volume. (c) The required mush thickness,  $h$ , and volume. (d) The resulting maximum change in mush porosity. All are plotted as a function of mush permeability,  $k$ . The values indicated by the circle fall within the sample-scale permeability estimated from the enclaves and with  $\phi_g$  no greater than the value at which bubbles are expected to be trapped within a crystal mush (Parmigiani *et al.* 2016). The maximum porosity change is expected to be 1 per cent here, which is well within the range of poroelastic behaviour (e.g. Karig & Hou 1992). Lower permeabilities than this value that *meets all requirements* require higher gas fractions to produce the proper rhyolite compressibility than are feasible. This is not the case for higher permeabilities, if one considers them viable based on the consideration of sample- versus field-scale permeabilities. All results shown are for a host rock shear modulus of  $G_c = 12$  GPa, which equates to an eruptive pressure change of 32 MPa, and an areal footprint of  $A = 60$  km $^2$ . We allow  $\alpha$  to vary with dark blue representing  $\alpha = 0.7$ , solid light blue as  $\alpha = 0.9$ , and dashed light blue as  $\alpha = 0.5$ .

volume of approximately  $0.4 \text{ km}^3$ . Thus, approximately  $21 \text{ km}^3$  of rhyolite would remain in storage. The aforementioned estimates are somewhat larger or smaller if one assumes a different value for the Biot–Willis coefficient (Fig. 6).

We also estimate the maximum change in mush porosity,  $\Delta\phi$ , in Fig. 6(d), which is the absolute maximum change in porosity over the course of the simulation (see Appendix B3). A maximum increase of 1 percent is anticipated under the aforementioned constraints. This falls within the range of porosity changes observed during recoverable deformation of unconsolidated granular materials with similar porosities as the enclaves (Karig & Hou 1992). Porosity changes are inversely correlated with permeability. At permeabilities less than  $\approx 2 \times 10^{-9} \text{ m}^2$ , predicted porosity changes are likely too large for the poroelastic assumption to hold. Thus, both the required vesicularity and the predicted porosity changes make solutions corresponding to permeabilities less than  $6.7 \times 10^{-9} \text{ m}^2$  unlikely. Instead, higher permeability solutions are preferred, if field-scale permeabilities are applicable.

## 6.2 Additional considerations on model limitations

We adopt an areal extent of the Cordón Caulle system of  $60 \text{ km}^2$ . Both smaller and larger areal footprints have been proposed (e.g. Delgado *et al.* 2016; Novoa *et al.* 2022). Smaller areas would result in minimum misfit combinations for sample-scale permeabilities that violate the maximum  $\phi_g$  constraint of 0.15. If permeabilities are indeed larger than  $6.7 \times 10^{-9} \text{ m}^2$  due to field scale effects, then smaller areas could still have viable solutions. Larger areal extents push the results further into the allowable regime, meaning smaller permeabilities ( $< 6.7 \times 10^{-9} \text{ m}^2$ ) would then be feasible. We chose the current geometry on the basis that the magma storage system would not extend outside of the Cordón Caulle graben.

The simulations were for a shear modulus of the host rock of 12 GPa, which is within the range of values used in previous studies of deformation at Cordón Caulle (Delgado *et al.* 2019; Novoa *et al.* 2022). The simulated deflation during the eruption consequently corresponds to a decrease in pressure of the crystal-poor rhyolite of 32 MPa, which is similar to the overpressures estimated by Novoa *et al.* (2022). The corresponding pressure increase associated with the inflationary deformation after the eruption is 7 MPa. For different shear moduli of the host rock the simulated pressure changes would also be different. However, for smaller shear moduli, the estimated values for  $S_s$  would require values of  $\phi_g$  that violate the aforementioned upper limit of 0.15.

Our simulations result in a smoothly decaying rate of inflation after the eruption. The LOS displacements (Fig. 1c) show some low amplitude higher order temporal variability superimposed on this long-term trend, which our model cannot explain. Assuming that these variations are indeed magmatic, then some additional processes would need to be invoked to explain these small variations on top of the broader inflationary trend. They could include, for example, transient changes in the hydraulic properties of the magmatic system (e.g. Le Mével *et al.* 2021), temporal variations in volatile content (Spang *et al.* 2022), or several diking episodes. For the latter there is however no seismic evidence (Delgado *et al.* 2016, 2018).

## 6.3 Is there a mush beneath Cordón Caulle?

Are the estimated volumes of the mush and overlying rhyolite reasonable, and do they support the potential existence of a crystal

mush beneath Cordón Caulle? If taken at face value, meaning that our estimates encompass the entire magma storage system beneath Cordón Caulle, they would be consistent with what has been inferred by Singer *et al.* (2008). Based on their synthesis, Cordón Caulle has erupted exclusively rhyolitic and rhyodacitic magmas since 32 ka, with half of the rhyolitic activity during the last 16.5 ka. In particular, the 1921–1922, the 1960, and the 2011–2012 rhyolites represent some of the most evolved magmas erupted in the entire Puyehue–Cordón Caulle complex, although it should be noted that the extent to which Puyehue and Cordón Caulle represent the same system remains unclear (Singer *et al.* 2008). Prior to the past 32 000 yr, that is between 173 and 32 ka, magmas were mainly basaltic and andesitic in composition, with a gap of  $>9$  wt per cent in  $\text{SiO}_2$  separating the older lavas from the later silicic ones. Jicha *et al.* (2007) found that the rhyolites produced by the entire complex may have fractionated from 85 per cent crystallization of a basaltic to a basaltic andesitic parent magma. Consequently, about  $130 \text{ km}^3$  of basaltic magma would have been required to produce  $14.5 \text{ km}^3$  of rhyolitic magma through fractional crystallization (Singer *et al.* 2008). We find a mush volume of  $60 \text{ km}^3$ , if we allow for sample-scale permeabilities only, which is about half of the total volume of basalt predicted by Singer *et al.* (2008). However, the possibility of field-scale permeabilities that are larger than permeabilities at the sample scale, or vertical stratification in mush properties, would result in volume estimates of  $130 \text{ km}^3$  or more.

If one takes a broader view of crystal mush systems which erupt crystal-poor silicic magmas it is feasible, albeit speculative, that our analysis only captures the upper parts of a vertically heterogeneous or stratified system that has been evolving as a consequence of deeper mafic magma supply and gravitationally driven segregation processes (Bachmann & Bergantz 2004; Hildreth 2004; Cashman *et al.* 2017). For example, one could speculate that the Cordón Caulle system at present is similar to the Long Valley system during its early Glass Mountain stage (Hildreth 2004, 2021). This invariably leads to the question of long-term thermal viability and evolution of the Cordón Caulle system. Hildreth (2021) considers that the longevity of the melt percolation process is favoured by several kilometres of permeable mush with hot mafic recharge from below. At the same time he leaves open whether rhyolite melt bodies that form atop a mush are thermally buffered for long time periods or whether they are intermittent features. Our model neither provides insight into the longer-term evolution of such a system, nor does it include the role of deeper magma supply. This is by design. The no-flow lower boundary condition for our model was chosen to provide the simplest model possible that can represent the short-term poroelastic response to eruptive magma withdrawal from the crystal-poor rhyolite.

A finite mush is also required by the poroelastic model because the rate of LOS uplift exponentially decays over time. Within the constraints of a poroelastic model and depth-invariant properties, this can only be achieved with a finite mush where the pore-pressure diffusion timescale is similar to the exponential decay timescale of the LOS uplift rate. In other words, the change in pore pressure that diffuses downward through the mush reaches the bottom no-flow boundary, and thereby causes the decay in the rate of observed uplift. For a mush that is sufficiently thick so that the pressure change does not reach the bottom boundary, the rate of uplift remains nearly constant throughout the simulation period, unless there is a decrease in permeability or increase in specific storage with depth. Here we assume mush properties that are spatially invariant, recognizing that any changes in properties with respect to depth would occur over

lengths that scale with the estimated mush thicknesses shown in Fig. 6(c).

Our results are for predicted changes in porosity of the order of 1 per cent (Fig. 6d), which is consistent with the observed poroelastic behaviour of unconsolidated granular materials (e.g. Karig & Hou 1992). As already discussed in Section 3, the potential relevance of poroviscoelastic or poroplastic behaviour may depend on the degree of sintering of crystals (Holness 2018), which provides impetus for further investigation of samples for evidence of such deformation. At present such evidence seems lacking (Winslow *et al.* 2022; Holness 2018).

The existence of the mafic enclaves with interstitial rhyolite points towards a primitive mush (Winslow *et al.* 2022). Much of the 85 per cent of chemical fractionation from crystallization of a basaltic to a basaltic andesitic magma envisioned by Jicha *et al.* (2007) is evident in the enclaves (Winslow *et al.* 2022). Since this primitive mush is presumably producing the rhyolite, little fractionation from deeper primitive melts is necessary. Thus, substantially deeper melt storage is not required to explain the recent events at Cerdón Caille. However, we do not discount recharge as an important component in this magmatic system, because the long-term viability of the system will of course depend on this (e.g. Gelman *et al.* 2013; Annen *et al.* 2015). In terms of thermal viability and long-term evolution of magma-mush systems (Gelman *et al.* 2013), we point to the existence of a large geothermal system at Cerdón Caille (Sepúlveda *et al.* 2005) for which Singer *et al.* (2008) proposed latent heat release from crystallization as a partial driver during the past 16.5 ka.

#### 6.4 Discriminating uplift models

Although we argue that the observed uplift at Cerdón Caille is a response to melt segregation from a magma mush, no direct geophysical observation of this process has been recorded (although the existence of the enclaves lend credence to this hypothesis). Our model is one of a few physical models that could explain the uplift, including models that invoke deeper seated recharge (Delgado *et al.* 2016) or viscoelastic relaxation of the host rock (Segall 2016). Like the model we have presented, viscoelastic relaxation also may not require recharge to produce uplift in specific circumstances (Segall 2016).

To differentiate between these possible mechanisms, future geophysical surveys could be completed, as each mechanism may have distinct signatures. For example, imaging the magma reservoir may be possible using gravity surveys (e.g. Flinders *et al.* 2013; Harpp & Geist 2018), magnetotelluric measurements (e.g. Samrock *et al.* 2021) and seismic tomography (e.g. Lees 2007), or combinations of these techniques (Pritchard & Gregg 2016), assuming a high enough resolution could be obtained. Results might show whether a mush exists beneath Cerdón Caille, possibly constrain its size, and also provide more information about the architecture of the greater Puyehue-Cerdón Caille system. Although these future measurements may help constrain deformation models, they cannot necessarily distinguish between one mechanism over another. For instance, the presence of a mush does not necessitate that poroelastic effects completely contribute to surface uplift. However, the lack of a mush would rule out this mechanism.

Temporal observations may provide more insight into underlying processes ongoing within the reservoir. Temporal changes in gravity may help determine causes of ongoing uplift (Battaglia *et al.* 2003;

Segall 2010). Recharge from deep should have a stronger positive gravity variation compared to either mush melt migration or viscoelastic relaxation. Recharge brings new mass into the reservoir, causing a relatively large positive variation, whereas mush melt migration only transports material a short distance, leading to a smaller gravitational change. Viscoelastic relaxation without recharge may induce an even smaller gravitational change after accounting for the deformation, as material is generally not being transported. Temporal gravity measurements may even discriminate the contribution of each mechanism to the observed deformation. Gas and thermal monitoring of the hydrothermal system also may help differentiate causes of inflation. Deep-sourced recharge may be more volatile rich and also hotter than rhyolitic melt percolating from the mush (Edmonds 2008).

Intriguingly, the post-eruptive uplift at Cerdón Caille has been nearly aseismic (Delgado *et al.* 2016, 2018). Delgado *et al.* (2018) invoked the Kaiser effect to explain the lack of seismicity (Heimisson *et al.* 2015), which predicts that any seismicity will remain low until the stress in the magmatic reservoir is close to the maximum value of the previous loading cycle (i.e. prior to eruption). Our model cannot help evaluate this hypothesis. One could ask though whether seismicity would be expected during poroelastic melt migration, in contrast to magma injection, which has been envisaged alternatively (Delgado *et al.* 2016, 2018). A possible alternate model for inflation at Cerdón Caille could be based on viscoelastic relaxation of the host rock (Segall 2016), although it is not clear whether this would be mostly aseismic. The uplift caused by the melt segregation from a crystal mush would, however, still require the Kaiser effect at least to explain the lack of seismicity within the host rocks. Future monitoring of the seismicity at Cerdón Caille, along with deformation, may help shed light on the ongoing processes.

## 7 CONCLUSIONS

The 2011–2012 eruption at Cerdón Caille was fed from a crystal-poor rhyolite body that should underlie a large part of the Cerdón Caille graben. Our analysis supports the possibility that post-eruptive uplift at Cerdón Caille may be due to recharge of this crystal-poor rhyolite magma reservoir, as a consequence of melt segregation from an underlying crystal mush, and in response to magma withdrawal from the rhyolite reservoir during the 2011–2012 eruption. Neither deeper recharge during the time period since the eruption ended (Delgado *et al.* 2016, 2018) nor alternate processes that give rise to inflationary deformation, such as viscoelastic relaxation of the host rock (Segall 2016), can be ruled out through our analysis. It is, however, possible to account for all of the uplift of the past decade through melt segregation from a magma mush.

The potential existence of such a mush is supported by the presence of mafic enclaves within the erupted rhyolite (Winslow *et al.* 2022). Moreover, crystal mush has been postulated as the source for evolved silicic magmas (Hildreth 2021), such as those that have been erupting at Cerdón Caille during the past 16.5 ka. In addition, the release of latent heat associated with the evolution of such a crystal mush would likely suffice to drive Cerdón Caille's geothermal system. Thus, multiple lines of reasoning support the potential existence of a crystal mush beneath Cerdón Caille. If this was indeed the case, then mush-derived recharge as envisaged and simulated herein would arguably be an inescapable consequence of the eruption.

Geometrically idealized 1-D modelling of this process, together with observational constraints, results in estimates of relevant parameters. In light of the many simplifications and assumptions, these estimates should be viewed as laden with uncertainty and are solely for the purpose of testing the feasibility of the mush hypothesis. Within that context, best estimates include a permeability of  $6.7 \times 10^{-9} \text{ m}^2$  for the mush, based on average grain sizes and porosities of the Cordón Caulle enclaves. Other parameter estimates are the specific storage of the mush with a value of  $4 \times 10^{-10} \text{ Pa}^{-1}$  and a mush thickness of approximately 1 km, corresponding to a volume of  $60 \text{ km}^3$ . The overlying rhyolite would correspondingly have a thickness of 260 m or a volume of  $15.6 \text{ km}^3$ . The corresponding increase in pressure of the crystal-poor rhyolite reservoir would be 7 MPa since the 2011–2012 eruption ended.

## ACKNOWLEDGMENTS

This work was supported by NSF-EAR 182425 to HMG, NSF-EAR 1823122 to PR and NSF-EAR 1824160 to MEP. Discussions with Kyle Anderson, Jacob Jordan and Cin-Ty Lee are appreciated. We also thank Christian Huber and Paul Segall for their insightful and valuable reviews.

## DATA AVAILABILITY

The data underlying this paper and the code used to produce it will be shared on request to the corresponding author.

## REFERENCES

- Anderson, K. & Segall, P., 2011. Physics-based models of ground deformation and extrusion rate at effusively erupting volcanoes, *J. geophys. Res.*, **116**(B7), doi:10.1029/2010JB007939.
- Annen, C., Blundy, J. & Sparks, R., 2006. The genesis of intermediate and silicic magmas in deep crustal hot zones, *J. Petrol.*, **47**(3), 505–539.
- Annen, C., Blundy, J.D., Leuthold, J. & Sparks, R. S.J., 2015. Construction and evolution of igneous bodies: towards an integrated perspective of crustal magmatism, *Lithos*, **230**, 206–221.
- Bachmann, O. & Bergantz, G.W., 2004. On the origin of crystal-poor rhyolites: extracted from batholithic crystal mushes, *J. Petrol.*, **45**(8), 1565–1582.
- Bachmann, O. & Huber, C., 2016. Silicic magma reservoirs in the Earth's crust, *Am. Mineral.*, **101**(11), 2377–2404.
- Bass, J.D., 1995. *Elasticity of Minerals, Glasses, and Melts*, pp. 45–63, American Geophysical Union (AGU).
- Battaglia, M., Segall, P. & Roberts, C., 2003. The mechanics of unrest at Long Valley Caldera, California. 2. Constraining the nature of the source using geodetic and micro-gravity data, *J. Volc. Geotherm. Res.*, **127**(3), 219–245.
- Bertin, D., Amigo, A., Lara, L.E., Orozco, G. & Silva, C., 2012. Erupción del Cordón Caulle 2011–2012: evolución fase efusiva, in *Proceedings of the XIII Congreso Geológico Chileno*, Antofagasta, pp. 539–541.
- Bertin, D., Lara, L., Basualto, D., Amigo, Á., Cardona, C., Franco, L., Gil, F. & Lazo, J., 2015. High effusion rates of the Cordón Caulle 2011–2012 eruption (Southern Andes) and their relation with the quasi-harmonic tremor, *Geophys. Res. Lett.*, **42**(17), 7054–7063.
- Biggs, J. & Pritchard, M.E., 2017. Global volcano monitoring: what does it mean when volcanoes deform?, *Elements*, **13**(1), 17–22.
- Biot, M.A., 1941. General theory of three-dimensional consolidation, *J. Appl. Phys.*, **12**(2), 155–164.
- Biot, M.A., 1956. General solutions of the equations of elasticity and consolidation for a porous material, *J. Appl. Phys.*, **23**(1), 91–96.
- Biot, M.A., 1973. Nonlinear and semilinear rheology of porous solids, *J. geophys. Res.*, **78**(23), 4924–4937.
- Biot, M.A. & Willis, D.G., 1957. The elastic coefficients of the theory of consolidation, *J. Appl. Mech.*, **24**(4), 594–601.
- Bonadonna, C., Cioni, R., Pistolesi, M., Elissondo, M. & Baumann, V., 2015a. Sedimentation of long-lasting wind-affected volcanic plumes: the example of the 2011 rhyolitic Cordón Caulle eruption, Chile, *Bull. Volcanol.*, **77**(2), 1–19.
- Bonadonna, C., Pistolesi, M., Cioni, R., Degruyter, W., Elissondo, M. & Baumann, V., 2015b. Dynamics of wind-affected volcanic plumes: the example of the 2011 Cordón Caulle eruption, Chile, *J. geophys. Res.*, **120**(4), 2242–2261.
- Carmichael, R.S., 1982. *Handbook of Physical Properties of Rocks*, Vol. II, CRC Press.
- Cashman, K.V., Sparks, R. S.J. & Blundy, J.D., 2017. Vertically extensive and unstable magmatic systems: a unified view of igneous processes, *Science*, **355**(6331), doi:10.1126/science.aag3055.
- Castro, J.M., Schipper, C.I., Mueller, S.P., Militzer, A., Amigo, A., Parejas, C.S. & Jacob, D., 2013. Storage and eruption of near-liquidus rhyolite magma at Cordón Caulle, Chile, *Bull. Volcanol.*, **75**(4), 702, doi:10.1007/s00445-013-0702-9.
- Castro, J.M., Cordonnier, B., Schipper, C.I., Tuffen, H., Baumann, T.S. & Feisel, Y., 2016. Rapid laccolith intrusion driven by explosive volcanic eruption, *Nat. Commun.*, **7**(1), 1–7.
- Cheadle, M., Elliott, M. & McKenzie, D., 2004. Percolation threshold and permeability of crystallizing igneous rocks: the importance of textural equilibrium, *Geology*, **32**(9), 757–760.
- Cheng, A. H.-D., 2016. *Poroelasticity, Vol. 27 of Theory and Applications of Transport in Porous Media*, Springer International Publishing.
- Clauser, C., 1992. Permeability of crystalline rocks, *EOS, Trans. Am. geophys. Un.*, **73**(21), 233–238.
- Coppola, D., Laiolo, M., Franchi, A., Massimetti, F., Cigolini, C. & Lara, L., 2017. Measuring effusion rates of obsidian lava flows by means of satellite thermal data, *J. Volc. Geotherm. Res.*, **347**, 82–90.
- Crozier, J. et al., 2022. Outgassing through magmatic fractures enables effusive eruption of silicic magma, *J. Volc. Geotherm. Res.*, **430**, doi:10.1016/j.jvolgeores.2022.107617.
- Delaney, P. & McTigue, D., 1994. Volume of magma accumulation or withdrawal estimated from surface uplift or subsidence, with application to the 1960 collapse of Kilauea volcano, *Bull. Volcanol.*, **56**(6), 417–424.
- Delgado, F., 2021. Rhyolitic volcano dynamics in the Southern Andes: contributions from 17 years of InSAR observations at Cordón Caulle volcano from 2003 to 2020, *J. South Am. Earth Sci.*, **106**, doi:10.1016/j.jsames.2020.102841.
- Delgado, F., Pritchard, M.E., Basualto, D., Lazo, J., Córdova, L. & Lara, L.E., 2016. Rapid reinflation following the 2011–2012 rhyodacite eruption at Cordón Caulle volcano (Southern Andes) imaged by InSAR: evidence for magma reservoir refill, *Geophys. Res. Lett.*, **43**(18), 9552–9562.
- Delgado, F., Pritchard, M., Samsonov, S. & Córdova, L., 2018. Renewed post-eruptive uplift following the 2011–2012 rhyolitic eruption of Cordón Caulle (Southern Andes, Chile): evidence for transient episodes of magma reservoir recharge during 2012–2018, *J. geophys. Res.*, **123**(11), 9407–9429.
- Delgado, F., Kubanek, J., Anderson, K., Lundgren, P. & Pritchard, M., 2019. Physicochemical models of effusive rhyolitic eruptions constrained with InSAR and DEM data: a case study of the 2011–2012 Cordón Caulle eruption, *Earth planet. Sci. Lett.*, **524**, doi:10.1016/j.epsl.2019.115736.
- Dvorak, J.J. & Dzurisin, D., 1997. Volcano geodesy: the search for magma reservoirs and the formation of eruptive vents, *Rev. Geophys.*, **35**(3), 343–384.
- Dzurisin, D., Lisowski, M., Wicks, C.W., Poland, M.P. & Endo, E.T., 2006. Geodetic observations and modeling of magmatic inflation at the Three Sisters volcanic center, central Oregon Cascade Range, USA, *J. Volc. Geotherm. Res.*, **150**(1), 35–54.
- Edmonds, M., 2008. New geochemical insights into volcanic degassing, *Phil. Trans. R. Soc. A*, **366**(1885), 4559–4579.
- Fletcher, C., 1998. *Computational Techniques for Fluid Dynamics 1: Fundamental and General Techniques*, Springer Berlin Heidelberg.

- Flinders, A.F., Ito, G., Garcia, M.O., Sinton, J.M., Kauahikaua, J. & Taylor, B., 2013. Intrusive dike complexes, cumulate cores, and the extrusive growth of Hawaiian volcanoes, *Geophys. Res. Lett.*, **40**(13), 3367–3373.
- Gelman, S.E., Gutiérrez, F.J. & Bachmann, O., 2013. On the longevity of large upper crustal silicic magma reservoirs, *Geology*, **41**(7), 759–762.
- Gudmundsson, A., 2012. Magma chambers: formation, local stresses, excess pressures, and compartments, *J. Volc. Geotherm. Res.*, **237**, 19–41.
- Harpp, K.S. & Geist, D.J., 2018. The evolution of Galápagos volcanoes: an alternative perspective, *Front. Earth Sci.*, **6**, 50, doi:10.3389/feart.2018.00050.
- Heimisson, E.R., Einarsson, P., Sigmundsson, F. & Brandsdóttir, B., 2015. Kilometer-scale Kaiser effect identified in Krafla volcano, Iceland, *Geophys. Res. Lett.*, **42**(19), 7958–7965.
- Hermes, O.D. & Cornell, W.C., 1981. Quenched crystal mush and associated magma compositions as indicated by intercumulus glasses from Mt. Vesuvius, Italy, *J. Volc. Geotherm. Res.*, **9**(2–3), 133–149.
- Hersum, T., Hilpert, M. & Marsh, B., 2005. Permeability and melt flow in simulated and natural partially molten basaltic magmas, *Earth planet. Sci. Lett.*, **237**(3–4), 798–814.
- Hickey, C. & Sabatier, J., 1997. Choosing Biot parameters for modeling water-saturated sand, *The Journal of the Acoustical Society of America*, **102**(3), 1480–1484.
- Hildreth, W., 1981. Gradients in silicic magma chambers: implications for lithospheric magmatism, *J. geophys. Res.*, **86**(B11), 10 153–10 192.
- Hildreth, W., 2004. Volcanological perspectives on Long Valley, Mammoth Mountain, and Mono Craters: several contiguous but discrete systems, *J. Volc. Geotherm. Res.*, **136**(3–4), 169–198.
- Hildreth, W., 2021. Comparative rhyolite systems: inferences from vent patterns and eruptive episodicities: eastern California and Laguna del Maule, *J. geophys. Res.*, **126**(7), e2020JB020879, doi:10.1029/2020JB020879.
- Hildreth, W. & Wilson, C.J., 2007. Compositional zoning of the Bishop Tuff, *J. Petrol.*, **48**(5), 951–999.
- Holness, M.B., 2018. Melt segregation from silicic crystal mushes: a critical appraisal of possible mechanisms and their microstructural record, *Contrib. Mineral. Petrol.*, **173**(6), 48, doi:10.1007/s00410-018-1465-2.
- Huber, C., Townsend, M., Degruyter, W. & Bachmann, O., 2019. Optimal depth of subvolcanic magma chamber growth controlled by volatiles and crust rheology, *Nat. Geosci.*, **12**(9), 762–768.
- Hui, H. & Zhang, Y., 2007. Toward a general viscosity equation for natural anhydrous and hydrous silicate melts, *Geochim. Cosmochim. Acta*, **71**(2), 403–416.
- Jay, J., Costa, F., Pritchard, M., Lara, L., Singer, B. & Herrin, J., 2014. Locating magma reservoirs using InSAR and petrology before and during the 2011–2012 Cordón Caulle silicic eruption, *Earth planet. Sci. Lett.*, **395**, 254–266.
- Jicha, B.R., Singer, B.S., Beard, B.L., Johnson, C.M., Moreno-Roa, H. & Naranjo, J.A., 2007. Rapid magma ascent and generation of 230Th excesses in the lower crust at Puyehue–Cordón Caulle, Southern Volcanic Zone, Chile, *Earth planet. Sci. Lett.*, **255**(1–2), 229–242.
- Karig, D.E. & Hou, G., 1992. High-stress consolidation experiments and their geologic implications, *J. geophys. Res.*, **97**(B1), 289–300.
- Kochenderfer, M.J. & Wheeler, T.A., 2019. *Algorithms for Optimization*, MIT Press.
- Kováčik, J., 2001. Correlation between shear modulus and porosity in porous materials, *J. Mater. Sci. Lett.*, **20**(21), 1953–1955.
- Lara, L., Moreno, H., Naranjo, J., Matthews, S. & De Arce, C.P., 2006. Magmatic evolution of the Puyehue–Cordón Caulle Volcanic Complex (40 S), Southern Andean Volcanic Zone: from shield to unusual rhyolitic fissure volcanism, *J. Volc. Geotherm. Res.*, **157**(4), 343–366.
- Le Mével, H., Córdova, L., Cardona, C. & Feigl, K., 2021. Unrest at the Laguna del Maule volcanic field 2005–2020: renewed acceleration of deformation, *Bull. Volcanol.*, **83**(6), 1–9.
- Lees, J.M., 2007. Seismic tomography of magmatic systems, *J. Volc. Geotherm. Res.*, **167**(1), 37–56.
- Liao, Y., Soule, S.A. & Jones, M., 2018. On the mechanical effects of poroelastic crystal mush in classical magma chamber models, *J. geophys. Res.*, **123**(11), 9376–9406.
- Liu, Y., Zhang, Y. & Behrens, H., 2005. Solubility of H<sub>2</sub>O in rhyolitic melts at low pressures and a new empirical model for mixed H<sub>2</sub>O–CO<sub>2</sub> solubility in rhyolitic melts, *J. Volc. Geotherm. Res.*, **143**(1–3), 219–235.
- Marchal, P., Hanotin, C., Michot, L. & de Richter, S.K., 2013. Two-state model to describe the rheological behavior of vibrated granular matter, *Phys. Rev. E*, **88**(1), doi:10.1103/PhysRevE.88.012207.
- Mullet, B. & Segall, P., 2022. The surface deformation signature of a transcrustal, crystal mush-dominant magma system, *J. geophys. Res.*, **127**(5), e2022JB024178, doi:10.1029/2022JB024178.
- Novoa, C. et al., 2022. The 2011 Cordón Caulle eruption triggered by slip on the Liquiñe-Ofqui fault system, *Earth planet. Sci. Lett.*, **583**, doi:10.1016/j.epsl.2022.117386.
- Okada, Y., 1992. Internal deformation due to shear and tensile faults in a half-space, *Bull. seism. Soc. Am.*, **82**(2), 1018–1040.
- Parmigiani, A., Faroughi, S., Huber, C., Bachmann, O. & Su, Y., 2016. Bubble accumulation and its role in the evolution of magma reservoirs in the upper crust, *Nature*, **532**(7600), 492–495.
- Pistolesi, M. et al., 2015. Complex dynamics of small-moderate volcanic events: the example of the 2011 rhyolitic Cordón Caulle eruption, Chile, *Bull. Volcanol.*, **77**(1), 1–24.
- Pritchard, M.E. & Gregg, P.M., 2016. Geophysical evidence for silicic crustal melt in the continents: where, what kind, and how much?, *Elements*, **12**(2), 121–127.
- Rice, J.R. & Cleary, M.P., 1976. Some basic stress diffusion solutions for fluid-saturated elastic porous media with compressible constituents, *Rev. Geophys.*, **14**(2), 227–241.
- Roeleffs, E., 1996. Poroelastic techniques in the study of earthquake-related hydrologic phenomena, *Adv. Geophys.*, **37**, 135–195.
- Saar, M.O., Manga, M., Cashman, K.V. & Fremouw, S., 2001. Numerical models of the onset of yield strength in crystal–melt suspensions, *Earth planet. Sci. Lett.*, **187**(3–4), 367–379.
- Sahimi, M., 1994. *Applications of Percolation Theory*, CRC Press.
- Samrock, F., Grayver, A.V., Bachmann, O., Özge, K. & Saar, M.O., 2021. Integrated magnetotelluric and petrological analysis of felsic magma reservoirs: insights from Ethiopian rift volcanoes, *Earth planet. Sci. Lett.*, **559**, doi:10.1016/j.epsl.2021.116765.
- Schipper, C.I., Castro, J.M., Tuffen, H., James, M.R. & How, P., 2013. Shallow vent architecture during hybrid explosive–effusive activity at Cordón Caulle (Chile, 2011–12): evidence from direct observations and pyroclast textures, *J. Volc. Geotherm. Res.*, **262**, 25–37.
- Schulze-Makuch, D., Carlson, D.A., Cherkauer, D.S. & Malik, P., 1999. Scale dependency of hydraulic conductivity in heterogeneous media, *Groundwater*, **37**(6), 904–919.
- Segall, P., 2010. *Earthquake and Volcano Deformation*, Princeton Univ. Press.
- Segall, P., 2016. Repressurization following eruption from a magma chamber with a viscoelastic aureole, *J. geophys. Res.*, **121**(12), 8501–8522.
- Selvadurai, A., 2021. On the poroelastic Biot coefficient for a granitic rock, *Geosciences*, **11**(5), 219, doi:10.3390/geosciences110502.
- Sepúlveda, F., Lahsen, A., Bonvalot, S., Cembrano, J., Alvarado, A. & Letelier, P., 2005. Morpho-structural evolution of the Cordón Caulle geothermal region, Southern Volcanic Zone, Chile: insights from gravity and 40Ar/39Ar dating, *J. Volc. Geotherm. Res.*, **148**(1), 165–189.
- Seropian, G., Schipper, C.I., Harmon, L.J., Smithies, S.L., Kennedy, B.M., Castro, J.M., Alloway, B.V. & Forte, P., 2021. A century of ongoing silicic volcanism at Cordón Caulle, Chile: new constraints on the magmatic system involved in the 1921–1922, 1960 and 2011–2012 eruptions, *J. Volc. Geotherm. Res.*, **420**, doi:10.1016/j.jvolgeores.2021.107406.
- Shinohara, H., 2008. Excess degassing from volcanoes and its role on eruptive and intrusive activity, *Rev. Geophys.*, **46**(4), doi:10.1029/2007RG000244.
- Singer, B.S., Jicha, B.R., Harper, M.A., Naranjo, J.A., Lara, L.E. & Moreno-Roa, H., 2008. Eruptive history, geochronology, and magmatic evolution of the Puyehue–Cordón Caulle volcanic complex, Chile, *Bull. geol. Soc. Am.*, **120**(5–6), 599–618.
- Song, I. & Renner, J., 2008. Hydromechanical properties of Fontainebleau sandstone: experimental determination and micromechanical modeling, *J. geophys. Res.*, **113**(B9), doi:10.1029/2007JB005055.

- Spang, A., Burton, M., Kaus, B.J. & Sigmundsson, F., 2022. Quantification of volcano deformation caused by volatile accumulation and release, *Geophys. Res. Lett.*, e2021GL097502, doi:10.1029/2021GL097502.
- Sparks, R., Annen, C., Blundy, J., Cashman, K., Rust, A. & Jackson, M., 2019. Formation and dynamics of magma reservoirs, *Phil. Trans. R. Soc., A*, **377**(2139), doi:10.1098/rsta.2018.0019.
- Sparks, R.S.J. & Cashman, K.V., 2017. Dynamic magma systems: implications for forecasting volcanic activity, *Elements*, **13**(1), 35–40.
- Toda, S., Stein, R.S., Sevilgen, V. & Lin, J., 2011. Coulomb 3.3 Graphic-rich deformation and stress-change software for earthquake, tectonic, and volcano research and teaching—user guide: U.S. Geological Survey Open-File Report 2011–1060, 63 pp., available at: <https://pubs.usgs.gov/of/2011/1060/>.
- Tuffen, H., James, M.R., Castro, J.M. & Schipper, C. I., 2013. Exceptional mobility of an advancing rhyolitic obsidian flow at Cordón Caulle volcano in Chile, *Nat. Commun.*, **4**(1), 1–7.
- Wallace, P., 2001. Volcanic SO<sub>2</sub> emissions and the abundance and distribution of exsolved gas in magma bodies, *J. Volc. Geotherm. Res.*, **108**(1–4), 85–106.
- Wang, H. F., 2000. *Theory of Linear Poroelasticity with Applications to Geomechanics and Hydrogeology*, Vol. 2, Princeton Univ. Press.
- Wendt, A., Tassara, A., Báez, J.C., Basualto, D., Lara, L.E. & García, F., 2017. Possible structural control on the 2011 eruption of Puyehue-Cordón Caulle Volcanic Complex (southern Chile) determined by InSAR, GPS and seismicity, *Geophys. J. Int.*, **208**(1), 134–147.
- Winslow, H. *et al.*, 2022. Insights for crystal mush storage utilizing mafic enclaves from the 2011–12 Cordón Caulle eruption, *Sci. Rep.*, **12**(1), 9734, doi:10.1038/s41598-022-13305-y.

## APPENDIX A: CONSTITUTIVE RELATIONSHIPS

First, the framework for poroelasticity is defined. This derivation will use the equations for linear poroelasticity as defined originally by Biot (1941), while generally keeping to the terminology defined in Wang (2000). The following methodology follows from Biot (1956), Biot & Willis (1957), Rice & Cleary (1976), Wang (2000), Cheng (2016) and Liao *et al.* (2018). In its simplest form, for an isotropic applied stress within principle coordinates, linear poroelasticity can be summarized by the two equations

$$\epsilon = a_{11}\sigma + a_{12}p \quad (\text{A1})$$

and

$$\zeta = a_{21}\sigma + a_{22}p. \quad (\text{A2})$$

Eq. (A1) defines the stress–strain relationship for a poroelastic solid. It states that any change in stress  $\sigma$  or pore fluid pressure  $p$  will cause a fractional volume change (strain,  $\epsilon$ ). Positive values of  $\sigma$  indicate compressive stress. Eq. (A2) is a requirement of eq. (A1). It specifies that a change in  $\sigma$  or  $p$  necessitates fluid to be added or removed from storage in the porous medium. This volume of fluid is defined as the increment in fluid content  $\zeta$ . Positive values of  $\zeta$  indicate fluid infiltrating the pore space. Finally, the constants are defined as

$$a = \begin{pmatrix} K^{-1} & H^{-1} \\ H^{-1} & R^{-1} \end{pmatrix}. \quad (\text{A3})$$

Three coefficients—drained compressibility ( $1/K$ ), poroelastic expansion coefficient ( $1/H$ ) and unconstrained specific storage coefficient ( $S_\sigma \equiv 1/R$ )—completely characterize the poroelastic response for an isotropic applied stress. The inverse of the drained bulk modulus,  $1/K$ , characterizes how the poroelastic matrix deforms due to a change in stress while keeping the pore pressure constant (drained). The term  $1/H$  describes how the bulk volume changes due to a

change in pore pressure. In hydrology,  $S_\sigma$  defines the volume of water released from storage per unit volume per unit decline in head while holding the stress constant. How eqs (A1) and (A2) are written is known as a pure compliance formulation since stress and pore pressure are *independent* variables. For our purposes, we will use a mixed stiffness formulation, which means stress and increment of fluid content are *dependent* variables. We can then set boundary conditions based on these variables, which will be discussed later. The isotropic stress equations using a mixed stiffness formulation are

$$\sigma = K\epsilon - \alpha p \quad (\text{A4})$$

and

$$\zeta = \alpha\epsilon + \frac{\alpha}{K_u B} p. \quad (\text{A5})$$

This introduces three new parameters, the Biot–Willis coefficient,  $\alpha$ , the undrained bulk modulus,  $K_u$  and Skempton’s coefficient,  $B$ . All of the coefficients come from algebraic manipulations of eq. (A1). A few important definitions are  $\alpha \equiv K/H$ ,  $B \equiv R/H$  and  $K_u \equiv K/(1 - \alpha B)$ . The term  $\alpha$  relates how much the pore volume changes due to fluid coming into or out of storage while keeping the pore pressure constant;  $K_u$  characterizes how much the bulk volume changes due to a change in stress while allowing the pore pressure to change (undrained) and  $B$  is the ratio of induced pore pressure to the change in applied stress for undrained conditions. Another definition for  $\alpha$  exists:

$$\alpha = 1 - \frac{K}{K'_s}. \quad (\text{A6})$$

Here the unjacketed bulk modulus ( $K'_s$ ) is introduced. It can be interpreted as the bulk modulus of the solid phase that makes up the matrix. This is only true if the matrix is a single phase. However, the assumption will be made that it is similar to a single grain’s bulk modulus. The combination of parameters in front of pore pressure in eq. (A5) is the constrained specific storage coefficient:

$$S_\epsilon \equiv \frac{\alpha}{K_u B} = \frac{\alpha^2}{K_u - K}. \quad (\text{A7})$$

$S_\epsilon$  is similar to  $S_\sigma$ , except it is measured at a constant strain (ergo constrained). The ratio of the two is equal to the ratio of the drained and undrained bulk moduli ( $S_\epsilon/S_\sigma = K/K_u$ ).

Eq. (A6) can be rearranged to solve for  $K$ ,

$$K = K'_s(1 - \alpha). \quad (\text{A8})$$

This leads to the definition of the undrained bulk modulus ( $K_u$ ), which takes  $K$ , the matrix bulk modulus, and adds the strength of the pores and pore fluids to it,

$$K_u = \frac{K}{1 - \alpha B}. \quad (\text{A9})$$

This becomes more apparent by substituting  $B = \alpha/(S_\epsilon K_u)$ ,

$$\begin{aligned} K_u &= \frac{K}{1 - \alpha^2/(S_\epsilon K_u)} \\ K_u - \frac{\alpha^2}{S_\epsilon} &= K \\ K_u &= K + \frac{\alpha^2}{S_\epsilon}. \end{aligned} \quad (\text{A10})$$

An expression for  $1/S_\epsilon$  can be introduced,

$$\frac{1}{S_\epsilon} = \frac{K_r K_s^2}{K_r(K_s - K_r) + \phi_0 K_s(K_s - K_r)}, \quad (\text{A11})$$

where  $\phi_0$  is the initial porosity and  $K_r$  is the pore fluid compressibility. Taking the definition of  $K$  from eq. (A8), this becomes

$$\begin{aligned} \frac{1}{S_\epsilon} &= \frac{K_r K_s^2}{K_r(K_s - K_s(1 - \alpha)) + \phi_0 K_s(K_s - K_r)} \\ &= \frac{K_r K_s}{K_r \alpha + \phi_0(K_s - K_r)} \\ &= \frac{K_r K_s}{\phi_0 K_s + (\alpha - \phi_0) K_r}. \end{aligned} \quad (\text{A12})$$

This result can be substituted into eq. (A10) to find

$$K_u = K + \frac{\alpha^2 K_s K_r}{\phi_0 K_s + (\alpha - \phi_0) K_r}. \quad (\text{A13})$$

These are the constants and equations necessary for the isotropic case.

For the 1-D case, which is the case for this model, the strain is in the vertical direction (uniaxial strain), meaning the isotropic stress case does not apply completely. A substitution can be made to eq. (A4) to compensate for this. By introducing the drained vertical incompressibility ( $K_v$ ) in place of  $K$  in eq. (A4), the equation becomes

$$\sigma = K_v \epsilon - \alpha p, \quad (\text{A14})$$

with

$$K_v = K + 4/3G. \quad (\text{A15})$$

By combining the drained bulk modulus and the shear modulus,  $K_v$  accounts for any strain arising from shear. This can be derived through manipulation of the mixed stiffness formulation of the non-principal coordinates equation:

$$\sigma_{ij} = \underbrace{2G\epsilon_{ij} + \left(K - \frac{2}{3}G\right)\epsilon_{kk}\delta_{ij}}_{\text{Poroelastic stress}} - \underbrace{\alpha p \delta_{ij}}_{\text{Free stress}} \quad (\text{A16})$$

$$\epsilon_{kk} = \epsilon_{xx} + \epsilon_{yy} + \epsilon_{zz}$$

$$\text{Uniaxial condition: } \epsilon_{xx} = \epsilon_{yy} = 0$$

$$\epsilon_{kk} = \epsilon_{zz}.$$

Only the stress in the  $z$  direction matters, so  $\sigma_{zz}$  can be solved for:

$$\sigma_{zz} = 2G\epsilon_{zz} + \left(K - \frac{2}{3}G\right)\epsilon_{zz} - \alpha p$$

$$\sigma_{zz} = \left(K + \frac{4}{3}G\right)\epsilon_{zz} - \alpha p. \quad (\text{A17})$$

Comparing this with eq. (A4), it takes the form of eq. (A14) with eq. (A15) substituted for  $K$ . As for  $\zeta$ , in the uniaxial case, it stays the same as eq. (A5).

One last relationship to discuss is how to define strain ( $\epsilon$ ). Generally, strain can be related to displacements as

$$\epsilon_{ij} = \frac{1}{2} \left( \frac{\partial u_i}{\partial x_j} + \frac{\partial u_j}{\partial x_i} \right), \quad (\text{A18})$$

or, for the uniaxial case,

$$\epsilon = \nabla \cdot u. \quad (\text{A19})$$

Eq. (A19) is what will be used throughout this derivation.

Finally, the change in pore fluid content ( $m$ ) can be substituted for  $\zeta$  using the initial fluid density as a constant of proportionality ( $m = \rho_0 \zeta$ ), allowing the equations to be in terms of changes in mass per unit volume rather than changes of volume per unit volume, which is useful when solving.

This leads to the final constitutive equations for stress and change in pore fluid content:

$$\sigma = K_v \nabla \cdot u - \alpha p \quad (\text{A20})$$

and

$$m = \rho_0 (\alpha \nabla \cdot u + S_\epsilon p). \quad (\text{A21})$$

## APPENDIX B: THE MODEL EQUATIONS

### B1 Diffusion equation

An assumption inherent to the constitutive equations is the lack of time dependence in the elastic response of the materials, particularly compared to how quickly fluid flows within the poroelastic material. Applied stresses instantaneously produce changes in fluid pressure and changes in fluid pressure instantaneously produce changes in volume. This is known as the quasistatic approximation. In other words, at any given time, there is no spacial gradient in stress. Mathematically, this is written as

$$\nabla \cdot \sigma = 0. \quad (\text{B1})$$

Taking the divergence of eq. (A20), leads to

$$\nabla \cdot \sigma = 0 = \nabla [K_v \nabla \cdot u - \alpha p]. \quad (\text{B2})$$

Since the gradient is always zero, the equation within the brackets must only depend on time. This time dependence ultimately comes from pressure changes due to fluid flow.

To derive an expression for this time dependence, one starts with the constitutive relationship for  $m$  (eq. A21) and takes the gradient,

$$\nabla m = \rho_0 (\alpha \nabla (\nabla \cdot u) + S_\epsilon \nabla p). \quad (\text{B3})$$

Taking eq. (B2) and solving for  $\nabla(\nabla \cdot u)$  gives

$$\nabla(\nabla \cdot u) = \frac{\alpha \nabla p}{K_v}. \quad (\text{B4})$$

Substituting this into the previous equation and solving for  $\nabla p$  gives

$$\begin{aligned} \nabla m &= \rho_0 \left( \frac{\alpha^2 \nabla p}{K_v} + S_\epsilon \nabla p \right) \\ &= \rho_0 \left[ \frac{\alpha^2}{K_v} + S_\epsilon \right] \nabla p. \end{aligned} \quad (\text{B5})$$

The uniaxial specific storage can be defined

$$\frac{\alpha^2}{K_v} + S_\epsilon \equiv S_s. \quad (\text{B6})$$

It represents the volume of fluid released per unit change in pressure per unit volume while keeping no lateral strain and constant vertical stress. Furthermore, the loading efficiency, the pore pressure increase due to a compressive axial stress increase while keeping the unit volume in a state of uniaxial strain, can be defined

$$\frac{\alpha}{S_s K_v} \equiv \gamma. \quad (\text{B7})$$

Therefore,

$$\nabla p = \frac{\nabla m}{\rho_0 S_s}. \quad (\text{B8})$$

Turning to Darcy's law,

$$q = -\frac{k}{\eta} \nabla p, \quad (\text{B9})$$

and conservation of mass,

$$\frac{\partial m}{\partial t} + \rho_0 \nabla \cdot q = 0, \quad (\text{B10})$$

provides two equations that govern fluid flow through the porous medium. Darcy's law states that the flux of fluid out of a porous material ( $q$ ) is proportional to the negative pressure gradient of the fluid. The two are related by the ratio of the permeability of the matrix to the viscosity of the fluid. The two can be combined by taking the divergence of Darcy's law and eliminating  $\nabla \cdot q$ .

$$\frac{\partial m}{\partial t} - \frac{\rho_0 k}{\eta} \nabla^2 p = 0. \quad (\text{B11})$$

Lastly, taking eq. (B8) and substituting in  $\nabla^2 p$  leads to a diffusion equation:

$$\frac{\partial m}{\partial t} = \frac{k}{\eta S_s} \nabla^2 m, \quad (\text{B12})$$

with an effective diffusivity,

$$c = \frac{k}{\eta S_s}. \quad (\text{B13})$$

## B2 Boundaries of the mush and initial condition

### B2.1 Bottom boundary

Assuming no material can cross into or out of the mush sets a no flux boundary condition. Physically, this means the bottom boundary is isolated from any injection of new material, and pore melt cannot flow out below. This can be done by setting the flux to zero in Darcy's law (eq. B9), giving

$$q = 0 = -\frac{k}{\eta} \nabla p \quad (\text{B14})$$

$$\nabla p = 0,$$

and by substituting eq. (B8) for  $\nabla p$  gives an expression in terms of  $m$ ,

$$\nabla m = 0. \quad (\text{B15})$$

If there is a flux into the mush at the bottom, then  $q$  can be non-zero, but that is beyond the scope of this investigation.

### B2.2 Upper boundary: change in rhyolite mass

After an eruption, the mass of the rhyolite layer will change with time depending on the amount entering from the mush ( $\Delta M_{\text{mush}}$ ) and the amount leaving the layer due to the eruption ( $\Delta M_{\text{E}}$ ):

$$\Delta M = \Delta M_{\text{mush}} - \Delta M_{\text{E}}. \quad (\text{B16})$$

One can express  $\Delta M_{\text{mush}}$  in terms of the total change in mass of the interstitial melt content of the mush  $m$  since the net change equals the amount leaked from the mush. This is written as

$$\Delta M_{\text{mush}} = -A \int_0^h m \, dz, \quad (\text{B17})$$

where  $h$  is the thickness of the mush. The negative sign comes from the convention that positive values of  $m$  indicate material entering the mush. By substituting this into eq. (B16) and taking the time derivative, the time rate of change of  $\Delta M$  becomes

$$\frac{dM}{dt} = -A \int_0^h \frac{\partial m}{\partial t} \, dz - Q, \quad (\text{B18})$$

where  $Q$  is the rate of mass erupted (e.g. Fig. 4). Substitution from eq. (2) gives

$$\frac{dM}{dt} = -Ac \left. \frac{\partial m}{\partial z} \right|_{z=h} - Q = A\rho_0 q_h - Q, \quad (\text{B19})$$

where  $q_h$  is the Darcy flux at the top of the mush from eq. (1) with  $m = \rho_0 \zeta$ . This must be multiplied by the cross sectional area ( $A$ ) to account for the 1-D flux. The change in mass can also be written according to the time dependent changes in volume and density,

$$\Delta M = \Delta(\rho V), \quad (\text{B20})$$

which can be linearized as

$$\Delta M = V_0 \Delta \rho + \rho_0 \Delta V. \quad (\text{B21})$$

The change in volume,  $\Delta V$ , is the difference between the final and initial volumes. The initial volume is simply the initial length of the rhyolite layer multiplied by  $A$ . The final volume depends on how much the top of the mush and the top of the rhyolite layer have moved,  $u_h$  and  $u_c$ , respectively. Increases in the top of the mush decrease the rhyolite thickness, whereas increases in the top of the rhyolite increase the thickness. In other words,

$$\Delta V = \underbrace{h_r + u_c - u_h}_{\text{final}} - \underbrace{h_r}_{\text{initial}} = A(u_c - u_h). \quad (\text{B22})$$

The displacement of the top of the rhyolite is related to the pressure of the rhyolite,  $P$ , by the transfer function  $\Psi_u \equiv du_c/dP$ , which depends on the geometry and the depth of the magma chamber as well as the physical properties of the rock surrounding the chamber. Thus,  $u_c = \Psi_u P$ . Based on the definition of the rhyolite compressibility ( $1/K_r$ ),

$$\frac{1}{K_r} = \frac{1}{\rho} \frac{\partial \rho}{\partial P}, \quad (\text{B23})$$

$\Delta \rho$  can be approximated as

$$\Delta \rho = \rho_0 \frac{P}{K_r}. \quad (\text{B24})$$

Taking the time derivative of eq. (B21) and substituting these previous expressions in gives

$$\begin{aligned} \frac{dM}{dt} &= V_0 \frac{d\rho}{dt} + \rho_0 \frac{dV}{dt} \\ &= Ah_r \frac{dP}{dt} \frac{\rho_0}{K_r} + \rho_0 A \frac{d(u_c - u_h)}{dt} \\ &= Ah_r \frac{dP}{dt} \frac{M_0}{K_r Ah_r} + \frac{M_0}{Ah_r} A \left( \Psi_u \frac{dP}{dt} - \frac{du_h}{dt} \right) \\ &= \frac{dP}{dt} \left( \frac{M_0}{K_r} + \frac{\Psi_u M_0}{h_r} \right) - \frac{M_0}{h_r} \frac{du_h}{dt}. \end{aligned} \quad (\text{B25})$$

Combining eqs (B19) and (B25) and solving for  $dP/dt$  gives

$$\begin{aligned} \frac{M_0}{Ah_r} q_h A - Q &= \frac{dP}{dt} \left( \frac{M_0}{K_r} + \frac{\Psi_u M_0}{h_r} \right) - \frac{M_0}{h_r} \frac{du_h}{dt} \\ \frac{dP}{dt} \left( \frac{1}{K_r} + \frac{\Psi_u}{h_r} \right) &= \frac{1}{h_r} q_h - \frac{Q}{M_0} + \frac{1}{h_r} \frac{du_h}{dt} \\ \frac{dP}{dt} &= \left[ \Psi_u + \frac{h_r}{K_r} \right]^{-1} \left[ q_h(t) - \frac{Q(t)}{\rho_0 A} + \frac{du_h}{dt} \right]. \end{aligned} \quad (\text{B26})$$

This defines how the pressure will change in the rhyolite layer, depending on the flux from the mush and the displacement of the top of the mush. The next steps are to find an equation for the displacement of the mush and relate the rhyolite layer pressure to  $m_h$ .

### B2.3 Upper boundary: mush displacement and $m$ to $P$ relationship

Recalling the quasistatic approximation, this gives a requirement for the top of the mush. Going back to eq. (A20),  $\sigma$  must be a purely time dependent function. This means the stress at the top of the mush is the same as the stress in the middle of the mush. Assuming stress continuity across the mush–rhyolite boundary,  $\sigma$  must be at all times

$$\sigma = -P. \quad (\text{B27})$$

Turning to eqs (A20) and (A21), equations for  $p$  and  $\nabla \cdot u$  can be derived. First, to get an equation for  $p$ , substitute  $\sigma = -P$ , while solving for and eliminating  $\nabla \cdot u$  from both equations,

$$\begin{aligned} \nabla \cdot u &= \frac{\alpha p - P}{K_v} \\ \nabla \cdot u &= \frac{m}{\rho_0 \alpha} - \frac{S_\epsilon P}{\alpha} \\ \frac{m}{\rho_0 \alpha} - \frac{S_\epsilon p}{\alpha} &= \frac{\alpha p - P}{K_v} \\ \left( \frac{\alpha}{K_v} + \frac{S_\epsilon}{\alpha} \right) p &= \frac{m}{\rho_0 \alpha} + \frac{P}{K_v} \\ p &= \frac{\frac{m}{\rho_0 \alpha} + \frac{P}{K_v}}{\frac{\alpha}{K_v} + \frac{S_\epsilon}{\alpha}} \cdot \frac{\alpha}{\alpha} \\ &= \frac{\frac{m}{\rho_0} + \frac{P \alpha}{K_v}}{\frac{\alpha^2}{K_v} + S_\epsilon} \\ &= \frac{1}{\rho_0 S_s} m + \frac{\alpha}{S_s K_v} P \\ p &= \frac{1}{\rho_0 S_s} m + \gamma P. \end{aligned} \quad (\text{B28})$$

To solve for  $\nabla \cdot u$ , substitute eq. (B28) into the first equation of the previous sequence,

$$\begin{aligned} \nabla \cdot u &= \frac{\alpha}{K_v} \left( \frac{1}{\rho_0 S_s} m + \frac{\alpha}{S_s K_v} P \right) - \frac{P}{K_v} \\ &= \frac{\alpha}{K_v S_s} \frac{m}{\rho_0} + \frac{\alpha^2}{K_v^2 S_s} P - \frac{P}{K_v} \\ &= \gamma \frac{m}{\rho_0} + \frac{P}{K_v} \left( \frac{\alpha^2}{K_v S_s} - 1 \right). \end{aligned} \quad (\text{B29})$$

To simplify the last term, recall  $S_s = \alpha^2/K_v + S_\epsilon$ ,

$$\begin{aligned} S_s &= \frac{\alpha^2}{K_v} + \frac{\alpha^2}{K_u - K} \\ &= \frac{\alpha^2(K_u - K + K_v)}{K_v(K_u - K)} \\ K_u - K + K_v &= \tilde{K}_v \\ \frac{1}{S_s} &= \frac{K_v}{\alpha^2} \left( \frac{K_u - K}{\tilde{K}_v} \right) \\ \frac{\alpha^2}{K_v} \frac{1}{S_s} &= \frac{\alpha^2}{K_v} \frac{K_v}{\alpha^2} \left( \frac{K_u - K}{\tilde{K}_v} \right). \end{aligned} \quad (\text{B30})$$

Substituting this back in,

$$\begin{aligned} \nabla \cdot u &= \gamma \frac{m}{\rho_0} + \frac{P}{K_v} \left( \frac{K_u - K}{\tilde{K}_v} - 1 \right) \\ &= \gamma \frac{m}{\rho_0} + \frac{P}{K_v} \left( \frac{K_u - K - K_u + 4/3G}{K_u + 4/3G} \right) \\ &= \gamma \frac{m}{\rho_0} + \frac{P}{K_v} \left( \frac{-K_v}{\tilde{K}_v} \right) \\ \nabla \cdot u &= \gamma \frac{m}{\rho_0} - \frac{P}{\tilde{K}_v}. \end{aligned} \quad (\text{B31})$$

Integrating eq. (B31) with respect to  $z$  over the thickness of the mush leads to

$$u_h = \frac{\gamma}{\rho_0} \int_0^h m dz - \frac{P}{\tilde{K}_v} \int_0^h dz. \quad (\text{B32})$$

Then, taking a derivative with respect to time,

$$\frac{du_h}{dt} = \frac{\gamma}{\rho_0} \int_0^h \frac{\partial m}{\partial t} dz - \frac{dP}{dt} \frac{h}{\tilde{K}_v}. \quad (\text{B33})$$

Recall that  $P$  only depends on  $t$ , so it only is affected by the time derivative and not the integration. Since  $\partial m/\partial t$  is being integrated across the entire mush, it can be replaced by the spacial derivative of the diffusion equation (eq. B12),

$$\begin{aligned} \frac{du_h}{dt} &= \frac{\gamma}{\rho_0} \int_0^h c \frac{\partial^2 m}{\partial z^2} dz - \frac{dP}{dt} \frac{h}{\tilde{K}_v} \\ &= \frac{\gamma}{\rho_0} c \nabla m_h - \frac{dP}{dt} \frac{h}{\tilde{K}_v}. \end{aligned} \quad (\text{B34})$$

In terms of  $q_h$ , this equation is also

$$\frac{du_h}{dt} = -\gamma q_h - \frac{h}{\tilde{K}_v} \frac{dP}{dt}. \quad (\text{B35})$$

With eqs (B26) and (B35), the upper boundary condition becomes:

$$\begin{aligned} \frac{dP}{dt} &= \left[ \Psi_u + \frac{h_r}{K_r} \right]^{-1} \left[ q_h - \frac{Q}{\rho_0 A} + -\gamma q_h - \frac{h}{\tilde{K}_v} \frac{dP}{dt} \right] \\ \frac{dP}{dt} \left[ \Psi_u + \frac{h_r}{K_r} \right] + \frac{dP}{dt} \frac{h}{\tilde{K}_v} &= q_h(1 - \gamma) - \frac{Q}{\rho_0 A} \\ \frac{dP}{dt} &= \left[ \Psi_u + \frac{h_r}{K_r} + \frac{h}{\tilde{K}_v} \right]^{-1} \left[ q_h(1 - \gamma) - \frac{Q}{\rho_0 A} \right], \end{aligned} \quad (\text{B36})$$

which we simplify further to

$$\frac{dP}{dt} = \frac{1}{\Omega} [q_h(1 - \gamma) - Q]. \quad (\text{B37})$$

Here,

$$\Omega = h_r \beta_{\text{eff}} = h_r \left( \frac{1}{K_r} + \frac{\Psi_u}{h_r} + \frac{h}{h_r \tilde{K}_v} \right) \quad (\text{B38})$$

with  $\beta_{\text{eff}}$  an effective compressibility of the crystal-poor rhyolite magma, and

$$Q(t) = \frac{1}{\rho_0 A} Q(t). \quad (\text{B39})$$

is the volumetric flux due to magma withdrawal.

A relationship between  $m_h$  and  $P$  can be derived from eq. (B28). At the top of the mush, assuming pressure continuity across the mush–rhyolite interface (i.e.  $p = P$ ) leads to

$$P = \frac{1}{\rho_0 S_s} m_h + \gamma P, \quad (\text{B40})$$

and after solving for  $m_h$ :

$$m_h = \rho_0 S_s (1 - \gamma) P. \quad (\text{B41})$$

#### B2.4 Upper boundary: in terms of $m$

The upper boundary condition can be expressed explicitly in terms of  $m$ . After combining eq. (B8) with eq. (B9), as well as eq. (B37) with eq. (B41), we find

$$\begin{aligned} \frac{dm_h}{dt} \frac{1}{\rho_0 S_s (1 - \gamma)} &= \frac{1}{\Omega} \left[ -\frac{c}{\rho_0} \frac{\partial m_h}{\partial z} (1 - \gamma) - \mathcal{Q} \right] \\ \frac{dm_h}{dt} &= -\frac{\rho_0 S_s (1 - \gamma)}{\Omega} \left[ \frac{c}{\rho_0} \frac{\partial m_h}{\partial z} (1 - \gamma) + \mathcal{Q} \right]. \end{aligned} \quad (\text{B42})$$

#### B2.5 Initial condition

With eqs (B12), (B15) and (B42), the entire mush system has been defined. An initial condition is now necessary to solve. For this problem, the mush and rhyolite layer are assumed to be stagnant at the beginning, meaning there are no gradients in pressure or in  $m$ . Therefore, the initial condition is

$$m(z, t = 0) = 0. \quad (\text{B43})$$

This indicates no flow is occurring in the mush.

### B3 Change in porosity

The predicted change in porosity allows one to assess whether poroelastic assumptions are holding. The change in porosity,  $\Delta\phi$ , is defined as

$$\Delta\phi = \phi_f - \phi_0, \quad (\text{B44})$$

where  $\phi_f$  is the final porosity. An expression for  $\phi_f$  can be derived by starting with the base definition of porosity:

$$\phi_f = \frac{V_f}{V}, \quad (\text{B45})$$

with  $V_f$  being the final volume of the pores and  $V$  being the final total volume of the mush. One can define  $V$  as the initial volume plus any change in the mush thickness,

$$V = A(h + u_h). \quad (\text{B46})$$

Since volume can be defined by density and mass,

$$V_f = \frac{M_f}{\rho_f} = \frac{M_0 - M_{\text{mush}}}{\rho_0 + \Delta\rho}, \quad (\text{B47})$$

where  $M_0$  is the initial mass of the pore fluid in the mush, which is  $\phi_0 \rho_0 V_0$ . Substituting B17 in for  $M_{\text{mush}}$  and approximating  $\Delta\rho$  gives

$$\begin{aligned} V_f &= \left[ \phi_0 \rho_0 V_0 + A \int_0^h m dz \right] \left[ \rho_0 + \rho_0 \frac{P}{K_r} \right]^{-1} \\ &= \left[ \phi_0 V_0 + \frac{A}{\rho_0} \int_0^h m dz \right] \left[ 1 + \frac{P}{K_r} \right]^{-1} \\ &= Ah \left[ \phi_0 + \frac{1}{h\rho_0} \int_0^h m dz \right] \left[ 1 + \frac{P}{K_r} \right]^{-1}. \end{aligned} \quad (\text{B48})$$

Dividing by the expression for  $V$  gives

$$\phi_f = \frac{h}{h + u_h} \left[ \phi_0 + \frac{1}{\rho_0 h} \int_0^h m dz \right] \left[ 1 + \frac{P}{K_r} \right]^{-1}. \quad (\text{B49})$$

Since  $u_h$  is small compared to  $h$ , the leading multiplicative term is approximately one. Therefore, the time dependent change in porosity can be approximated as

$$\Delta\phi = \left[ \phi_0 + \frac{1}{\rho_0 h} \int_0^h m dz \right] \left[ 1 + \frac{P}{K_r} \right]^{-1} - \phi_0. \quad (\text{B50})$$

### B4 Mass balance

The mass leaked from the mush has been defined two ways: using the Darcy flux of melt out of the top of the mush (eq. B19) and based on the total change in pore fluid content integrated over the mush (eq. B17). Ideally, these values will be equal at every time step, however, numerical error makes this not often the case. The mass balance equation is thus

$$\begin{aligned} -A \int_0^h m(t) dz &= \rho_0 A \int_0^t q dt \\ \int_0^h m(t) dz &= -\rho_0 \int_0^t q dt. \end{aligned} \quad (\text{B51})$$

### B5 Non-dimensionalization

All previous equations have been in dimensional form. The dimensionality components are

$$z = z'h \quad m = m'\rho_0 \quad t = t' \frac{h^2}{c} \quad (\text{B52})$$

where primes indicate non-dimensional variables. Substituting these into eqs (B12), (B15) and (B42),

$$\begin{aligned} \frac{\partial m'}{\partial t'} \frac{\rho_0 c}{h^2} &= c \frac{\rho_0}{h^2} \frac{\partial^2 m'}{\partial z'^2} \\ \frac{\partial m'}{\partial t'} &= \frac{\partial^2 m'}{\partial z'^2}; \end{aligned} \quad (\text{B53})$$

$$\begin{aligned} \frac{\partial m'}{\partial z'} \Big|_{z=0} \frac{\rho_0}{h} &= 0 \\ \frac{\partial m'}{\partial z'} \Big|_{z=0} &= 0; \end{aligned} \quad (\text{B54})$$

$$\begin{aligned} \frac{dm'_h}{dt'} \frac{\rho_0 c}{h^2} &= -\frac{\rho_0 S_s (1 - \gamma)}{\Omega} \left[ \frac{c}{\rho_0} \frac{\rho_0}{h} \frac{\partial m'_h}{\partial z'} (1 - \gamma) + \mathcal{Q} \right] \\ \frac{dm'_h}{dt'} &= -\frac{S_s (1 - \gamma)}{\Omega} \left[ \frac{ch^2}{c} \frac{1}{h} \frac{\partial m'_h}{\partial z'} (1 - \gamma) + \frac{h^2}{c} \mathcal{Q} \right] \\ \frac{dm'_h}{dt'} &= -\frac{S_s (1 - \gamma)}{\Omega} \left[ h(1 - \gamma) \frac{\partial m'_h}{\partial z'} + \tau \mathcal{Q} \right]. \end{aligned} \quad (\text{B55})$$

## APPENDIX C: DETAILS OF PARAMETER ESTIMATION

### C1 Parameters

#### C1.1 Bulk modulus of the crystal matrix, $K_s$

One can constrain  $K_s$  based on the phase proportions seen in thin sections and in back scatter electron images of the mafic enclaves (Winslow *et al.* 2022). The crystal content of the enclaves, expressed in terms of volume fraction, ranges from approximately 0.55–0.70. Crystals consist predominantly of phenocrysts as well as subordinate microlites that are interpreted to have formed as the enclaves

were erupted (Winslow *et al.* 2022). The phenocrysts are dominantly plagioclase, olivine, and clinopyroxene (with minor Fe–Ti oxide), at relative proportions of 0.64, 0.2 and 0.16, respectively. We can estimate  $K_s$  using the bulk moduli of each phenocryst phase (Biot 1941; Bass 1995). These are 72 GPa for  $\text{An}_{56}$ , 130 GPa for olivine and 105 GPa for clinopyroxene (a value between augite and diopside). We thus estimate a bulk modulus of  $K_s = 87.6$  GPa based on an average of these bulk moduli weighted by the phase proportions, which is the limit that assumes all grains deform equally (Hickey & Sabatier 1997).

### C1.2 Mush porosity, $\phi_0$ , and permeability, $k$

We define porosity,  $\phi_0$ , as the volume fraction of enclave not occupied by phenocrysts and estimate an average value of  $\phi_0 = 0.36$  from the volume fraction of crystals within the enclaves (Winslow *et al.* 2022). From  $\phi_0$  and the average maximum crystal dimension,  $a$ , we can constrain the mush permeability,  $k$ , from empirical relations between porosity and permeability of partially crystallized magmas (Cheadle *et al.* 2004; Hersum *et al.* 2005). Here we follow Hersum *et al.* (2005) and use the relation

$$k = \frac{1}{6.89} a^2 \phi_0^{4.37}. \quad (\text{C1})$$

The range in crystal sizes of the enclaves is approximately 1 mm  $\leq a \leq$  2 mm, which results in  $k = 1.7 \times 10^{-9}$  m<sup>2</sup> to  $6.7 \times 10^{-9}$  m<sup>2</sup>.

### C1.3 Shear modulus of the mush, $G$

The shear modulus of the crystal mush,  $G$ , is estimated based on the work of Kováčik (2001) as

$$G = G_0 \left( 1 - \frac{\phi_0}{\phi_c} \right)^f. \quad (\text{C2})$$

Here,  $G_0$  is the shear modulus of the material that comprises the solid matrix,  $\phi_c$  is the porosity at which the shear modulus goes to zero, and  $f$  is a material dependent exponent. From percolation theory,  $f$  is predicted to be 2.1 (Sahimi 1994), although in practice it typically falls between 1 and 2 (Kováčik 2001). We therefore use a value of  $f = 1.5$ . Furthermore, we use  $G_0 = 44$  GPa, which is for gabbro (Carmichael 1982) and  $\phi_c = 0.6$ , which corresponds to the threshold of crystal network formation (Saar *et al.* 2001; Bachmann & Bergantz 2004). Given that  $\phi_0 = 0.36$ , we obtain  $G = 11.2$  GPa.

### C1.4 Biot–Willis coefficient, $\alpha$

The Biot–Willis coefficient,  $\alpha$ , describes the relation between the change in the volume of fluid stored within the porous material to the change in the material's volume under constant pore pressure. Generally,  $\alpha = 1 - K/K_s$ . Note that  $K$  will always be less than  $K_s$  because pores will reduce the strength of the material. Therefore, for an incompressible solid ( $K_s \rightarrow \infty$ ) one has  $\alpha \rightarrow 1$ . Alternatively, if porosity tends towards zero,  $\alpha \rightarrow 0$ . Here we assume  $\alpha = 0.7 \pm 0.2$  which, for reference, falls within the range of sandstone at similar pressures (Song & Renner 2008) and porosities (Selvadurai 2021).

### C1.5 Rhyolite bulk modulus, $K_r$ , and volatile fraction, $\phi_g$

Although  $S_s$  has a physical definition based on bulk moduli (see Table 1 and Section C1.6), we will treat it as a dependent parameter.

As such, changes in  $S_s$  are driven by changes in  $K_r$ , which is the bulk modulus of the mixture of melt with volatile bubbles and depends on the bubble fraction within the interstitial melt,  $\phi_g$ , as well as the bubble compressibility (eq. 7). Approximating the volatile phase as an ideal gas, its compressibility is given by  $1/P_{\text{ref}}$ . Based on Jay *et al.* (2014) and Seropian *et al.* (2021), we assume  $P_{\text{ref}} = 140$  MPa. We further assume a bulk modulus for the melt of  $K_{\text{melt}} = 13$  GPa (Bass 1995). Finally, based on the work of Parmigiani *et al.* (2016), the largest bubble fraction that can likely remain trapped in a mush by capillary forces is  $\phi_g \approx 0.15$ . Using these values in eq. (7) gives  $K_r \approx 8.8 \times 10^8$  Pa.

### C1.6 Uniaxial specific storage, $S_s$

The storage capacity of the mush generally defines how much melt is added or released from ‘storage’ as a consequence of a change in the pressure of the pore fluid. Specifically, the uniaxial specific storage,  $S_s$ , is thus the volume of melt released, per volume of mush, per unit decrease in pore pressure, assuming a constant vertical stress and negligible horizontal strain. It encapsulates the combined compressibilities of the mush matrix and of the interstitial rhyolite melt with volatile bubbles, and it is a key unknown parameter that we seek to estimate. It is given by

$$S_s = \frac{\phi_0}{K_r} + \frac{\alpha - \phi_0}{K_s} + \frac{\alpha^2}{K_v}. \quad (\text{C3})$$

### C1.7 Melt viscosity, $\eta$ , and density, $\rho_0$

We estimate the viscosity of the Cordón Caulle rhyolite melt as  $\eta \approx 3300$  Pa·s. Our estimate uses the viscosity model of Hui & Zhang (2007) for the known rhyolite composition (Castro *et al.* 2013), a temperature of 908 °C (Jay *et al.* 2014) and a H<sub>2</sub>O content of 4.6 wt per cent (Liu *et al.* 2005), assuming H<sub>2</sub>O saturation at a pressure of 140 MPa (Jay *et al.* 2014; Seropian *et al.* 2021). We use a melt density of  $\rho_0 = 2300$  kg m<sup>-3</sup> (Castro *et al.* 2013).

### C1.8 Areal extent of the Cordón Caulle magmatic system, $A$

Based on the work of Delgado *et al.* (2016) and Novoa *et al.* (2022), most of the Cordón Caulle graben may be underlain by a magma storage complex (Lara *et al.* 2006). This is also consistent with the surface deformation during and after the eruption and estimates for the area encompassed by magma storage,  $A$ , obtained from geodetic inversions range from 20 to 200 km<sup>2</sup> (Delgado *et al.* 2016; Novoa *et al.* 2022). Herein we assume a rectangular sill-like storage reservoir located within the Cordón Caulle graben and with an areal extent of 60 km<sup>2</sup> (Fig. 1b) and an aspect ratio of 5 (Delgado *et al.* 2016). The ramifications of assuming different areal footprints of Cordón Caulle's magmatic system are discussed in Section 6.2.

### C1.9 Depth of the rhyolite layer, $d$

An important parameter in the sill model (Okada 1992), upon which the transfer functions  $\Psi_u$  and  $\Psi_w$  are based, is the depth to the top of the rhyolite layer,  $d$ . We use a value of 6 km based on prior estimates (Delgado *et al.* 2016; Novoa *et al.* 2022).

### C1.10 Mush and rhyolite thicknesses

Neither the mush thickness,  $h$ , nor the rhyolite thickness,  $h_r$  are known. Instead, both are estimated.

### C1.11 Host rock shear modulus and transfer functions

We use a shear modulus for the host rock,  $G_c$ , that ranges from more brittle and fractured rocks (1 GPa) to moderately strong rocks (35 GPa) all of which may be reasonable at Cordón Caulle (Wendt *et al.* 2017; Delgado *et al.* 2019; Novoa *et al.* 2022). We use these values of  $G_c$  together with a Poisson's ratio of 0.25 to calculate  $\Psi_u$  and  $\Psi_w$  using the sill model of Okada (1992) (see Section 4.3.1 for details). The resultant transfer functions have values of  $1.3 \times 10^{-7} \leq \Psi_u \leq 4.6 \times 10^{-6} \text{ m}\cdot\text{Pa}^{-1}$  and  $\Psi_w = 0.3324$  for the  $A = 60 \text{ km}^2$  reservoir.

### C1.12 Misfit in $S_s$ - $\eta/k$ space

After an exploratory random sampling of all parameters within a predefined range, we found that for any combination of parameters there is a unique value of both  $S_s$  and  $\eta/k$  for which the misfit  $\chi$  is the smallest. For some combinations of parameters the smallest value of  $\chi$  found within  $S_s$ - $\eta/k$  space corresponds to the minimum in  $\chi$  that can be achieved for any combination of parameters. We denote this value as  $\chi_{\min}$ . For other combinations of parameters the smallest value of  $\chi$  achievable within  $S_s$ - $\eta/k$  space is larger than  $\chi_{\min}$  and will be denoted as  $\chi_{\text{opt}}$ .

Figs C1 and C2 illustrate the difference between  $\chi_{\min}$  and  $\chi_{\text{opt}}$ . They are based on grid searches over  $S_s$  and  $\eta/k$  in the vicinity of the smallest misfit. The value of  $\chi$  is indicated by the colour, the lighter the colour the lower the misfit. The centre graphs of both Figs C1 and C2 are identical and serve as the reference case with the smallest value of  $\chi$  corresponding to  $\chi_{\min}$ . Each of the other graphs in either figure corresponds to a change in one parameter, as labelled on the graph, relative to the reference case. The corresponding smallest value in  $\chi$  for each case differs and is larger than  $\chi_{\min}$  of the reference case and will be referred to as  $\chi_{\text{opt}}$ .

### C1.13 Finding the parameters that give a minimum misfit

The values of  $\chi_{\text{opt}}$ , which are obtained from a random sampling of all parameters and minimization over  $S_s$  and  $\eta/k$ , can be shown to have well defined functional dependencies. These functional dependencies are expressed in terms of three functions,  $\Gamma_1$ ,  $\Gamma_2$  and  $\Gamma_3$ , and are shown in Fig. C3 as graphs of  $\chi_{\text{opt}}$  versus  $\Gamma_i$ . The small insets in Fig. C3 correspond to the minimum misfit,  $\chi_{\min}$ , and the optimized misfit,  $\chi_{\text{opt}}$ , cases. Each point shown in Fig. C3 represents one parameter combination that results in a misfit of  $\chi_{\text{opt}}$ , as for example case  $\mathcal{F}$  in Fig. 5(b). Some of these have a value of  $\chi_{\text{opt}} = \chi_{\min}$ , as for example case  $\mathcal{A}$  in Fig. 5(b).

It should be noted that the three  $\Gamma_i$  encompass the three unknown parameters  $S_s$ ,  $h$  and  $h_r$ . It is therefore possible to leverage these functional relations to find which parameter combinations yield the minimum misfit of  $\chi_{\min} = 3.75 \text{ cm}$ . Specifically, for a given set of *a priori* parameters that are either constrained to a specific value or to within a defined range (Table 1), we seek to find those combinations of  $S_s$ ,  $h$  and  $h_r$  that have  $\chi_{\min}$  as the smallest misfit in  $S_s$ - $\eta/k$  space. To do so we define three second order polynomials that each fit one of the  $\chi_{\text{opt}}$  versus  $\Gamma_i$  trends in Fig. C3. Taking the vertex of each polynomial as  $\Gamma_i = \Gamma_{i,\text{min}}$ , we then algebraically solve for the three unknowns  $S_s$ ,  $h$  and  $h_r$  where  $\chi_{\text{opt}} = \chi_{\min} = 3.75 \text{ cm}$ .

## C2 Derivation of $\Gamma_i$ functions

### C2.1 $\Gamma_1$

To obtain  $\Gamma_1$ , we turn to the long-term behaviour of the system. At the (hypothetical) steady state, all gradients in pressure and  $m$  will have relaxed to the values  $P_{ss}$  and  $m_{ss}$ , respectively. To find these values, we start with the pressure boundary condition (eq. B37) and integrate over time from 0 to infinity:

$$\int_0^\infty \frac{dP}{dt} dt = \frac{1}{\Omega} \left[ (1 - \gamma) \int_0^\infty q_h dt - \int_0^\infty \frac{Q}{\rho_0 A} \right]. \quad (\text{C4})$$

The left-hand side will simply become  $P_{ss}$ . From mass balance (eq. B51), the integral over  $q_h$  can be replaced with

$$\int_0^\infty q_h dt = -1/\rho_0 \int_0^h m dz = -m_{ss}/\rho_0 \int_0^h dz = -m_{ss}h/\rho_0. \quad (\text{C5})$$

Finally, as the eruptive flux goes to zero at the end of the eruption, the time integral over  $Q$  gives the total mass erupted,  $M_E^\infty$ . Eq. (C4) thus becomes

$$P_{ss} = -\frac{1}{\Omega} \left[ \frac{m_{ss}(1 - \gamma)h}{\rho_0} + \frac{M_E^\infty}{\rho_0 A} \right]. \quad (\text{C6})$$

Taking the relationship between  $P$  and  $m_h$  from eq. (B41), at steady state it becomes

$$m_{ss} = \rho_0 P_{ss} S_s (1 - \gamma), \quad (\text{C7})$$

which can be substituted into eq. (C6) for  $m_{ss}$  to get

$$P_{ss} = -\frac{1}{\Omega} \left[ \frac{(1 - \gamma)h\rho_0 S_s (1 - \gamma)P_{ss}}{\rho_0} - \frac{M_E^\infty}{\rho_0 A} \right]. \quad (\text{C8})$$

After simplifying and distributing  $1/\Omega$ , we find

$$P_{ss} = -\frac{S_s(1 - \gamma)^2 h}{\Omega} P_{ss} + \frac{-M_E^\infty}{\rho_0 \Omega A}. \quad (\text{C9})$$

$P_E$

Each term in this equation has units of pressure, thus we define the second term on the right-hand side as the instantaneous eruptive pressure change,  $P_E$ . To understand why this is a pressure, consider the definition of compressibility:

$$\beta = \frac{1}{\rho} \frac{\partial \rho}{\partial P} \quad \text{or} \quad \Delta P \approx \frac{\Delta \rho}{\rho \beta}. \quad (\text{C10})$$

Recalling that  $\Omega = h_r \beta_r$ , since  $M_E^\infty/(h_r A)$  is a change mass per volume it approximates an average change in density of the rhyolite layer. Solving for  $P_{ss}$  in eq. (C9) gives

$$P_{ss} \left[ 1 + \frac{S_s(1 - \gamma)^2 h}{\Omega} \right] = P_E, \quad (\text{C11})$$

and rearranging for the ratio of  $P_{ss}/P_E$  shows where  $\Gamma_1$  comes into the long-term behaviour of the system:

$$\frac{P_{ss}}{P_E} = \frac{1}{1 + S_s(1 - \gamma)^2 h/\Omega} = \frac{1}{1 + \Gamma_1}. \quad (\text{C12})$$

Although the primary purpose of considering the long-term behaviour has been to explain the origin of  $\Gamma_1$ , we also now have an expression that allows us to predict the long-term pressure change and thus surface deformation.

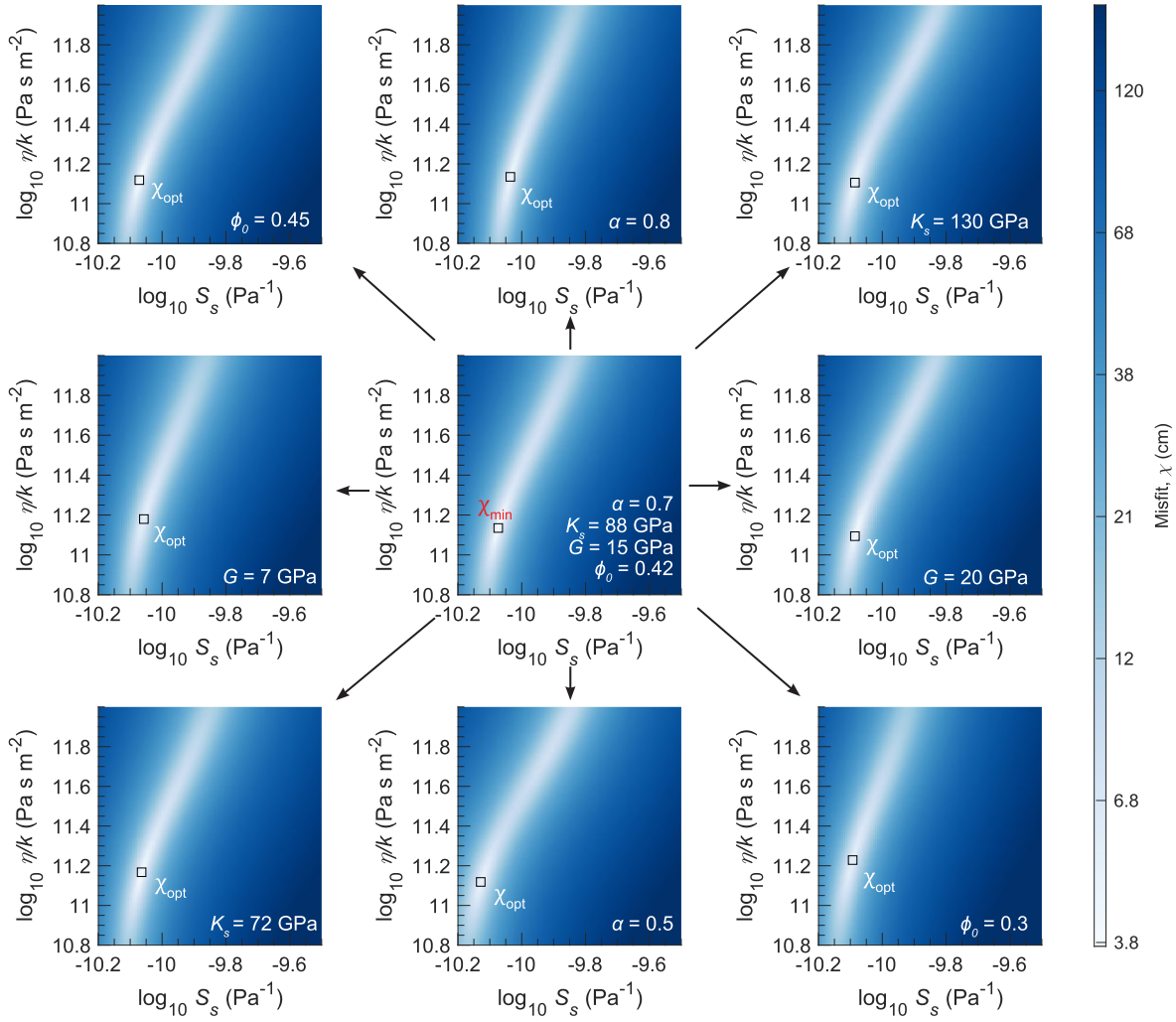


**Figure C1.** Misfit,  $\chi$ , as a function of  $S_s$  and  $\eta/k$  on a 100 by 100 grid for different combinations of parameters. Darker blue indicates larger misfit. At the centre is the reference case with values of  $\alpha = 0.7$ ,  $K_s = 88$  GPa,  $G = 15$  GPa and  $\phi_0 = 0.42$ . All other plots have one of these four parameters changed, relative to this reference case, as labelled. Other parameters were held constant at  $h = 4400$  m,  $h_r = 420$  m,  $\Psi_u = 3 \times 10^{-7}$  m Pa $^{-1}$  and  $\Psi_w = 0.46$ .

### C2.2 $\Gamma_2$

The second function,  $\Gamma_2$ , is simply the characteristic timescale for pore pressure diffusion within a porous medium, previously denoted as  $\tau$ .

### C2.3 $\Gamma_3$

The third function,  $\Gamma_3$ , is derived from the mush-rhyolite boundary condition by combining eqs (11) and (15), which gives

$$\frac{dm_h}{dt} = -\frac{S_s(1-\gamma)}{\Omega} \left[ (1-\gamma) \frac{c}{\rho_0} \frac{\partial m_h}{\partial z} + \frac{Q}{\rho_0 A} \right]. \quad (\text{C13})$$

Taking the surface displacement equation (eq. 16) and writing it terms of  $m_h$  using eq. (15) leads to

$$w = m_h \frac{\Psi_u \Psi_w}{\rho_0 S_s (1-\gamma)}. \quad (\text{C14})$$

After taking the time derivative of eq. (C14), we substitute eq. (C13) in for an expression of how the surface displacement changes with time:

$$\frac{dw}{dt} = -\frac{\Psi_u \Psi_w}{\Omega} \left[ (1-\gamma) \frac{c}{\rho_0} \frac{dm_h}{dz} + Q \right]. \quad (\text{C15})$$

The leading term in this equation, when scaled by  $1/A$  is the definition for  $\Gamma_3$ , which is invariant with area and results in the relationship with  $\chi_{\text{opt}}$  shown in Fig. C3(c). We obtain the same relationship if we were to define  $\Psi_w$  in terms of a volume change, rather than a pressure change. In other words,  $\Gamma_3 = \Psi_u \Psi_w / (\Omega A)$  is the response function that scales the rate of change in uplift to the rate of change in magma stored within the rhyolite layer.

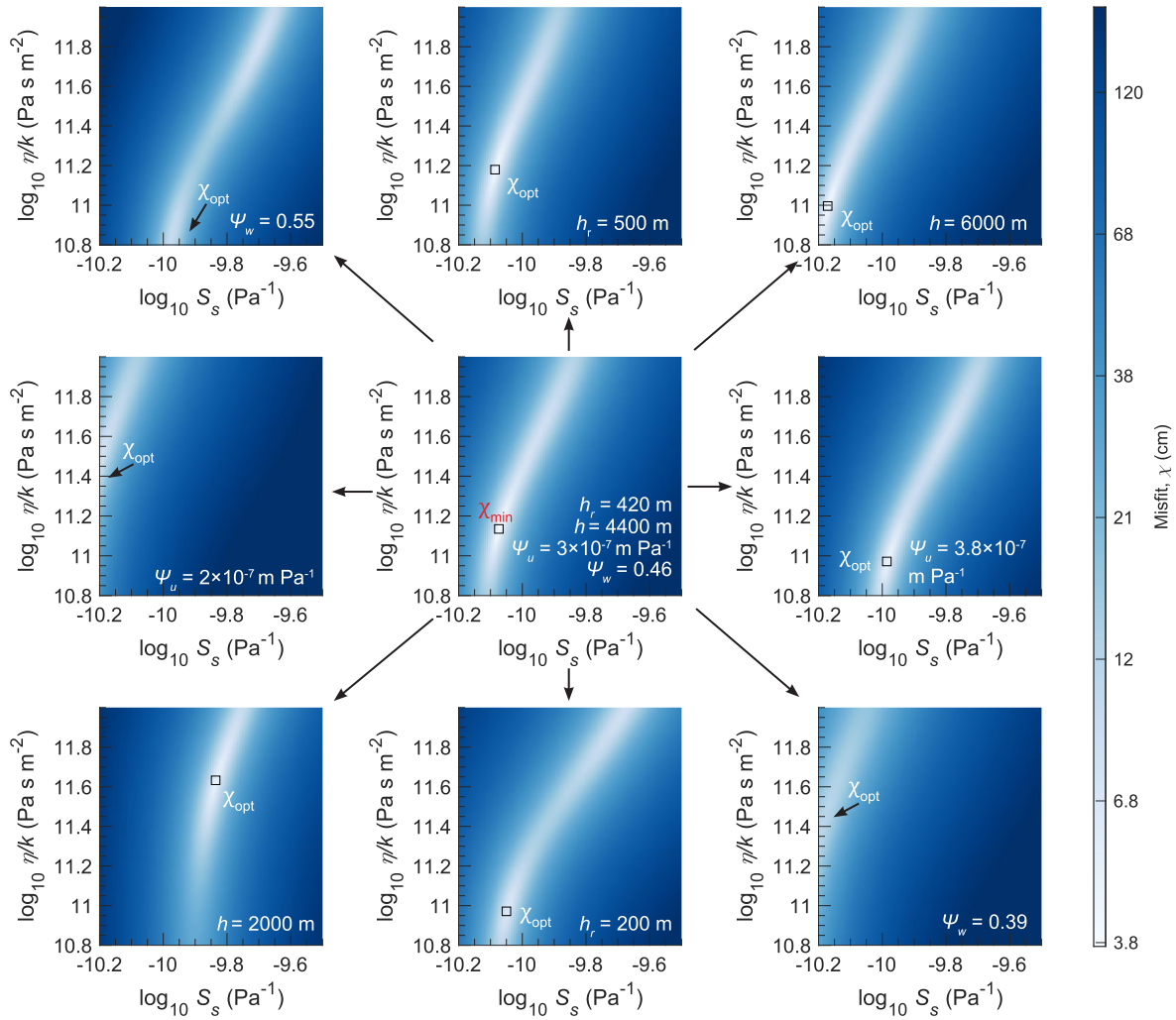


**Figure C2.** Misfit,  $\chi$ , as a function of  $S_s$  and  $\eta/k$  on a 100 by 100 grid for different combinations of parameters. Darker blue indicates larger misfit. At the centre is the reference case with values of  $h = 4400$  m,  $h_r = 420$  m,  $\Psi_u = 3 \times 10^{-7}$  m Pa $^{-1}$  and  $\Psi_w = 0.46$ . All other plots have one of these four parameters changed, relative to this reference case, as labelled. Other parameters were held constant at  $\alpha = 0.7$ ,  $K_s = 88$  GPa,  $G = 15$  GPa and  $\phi_0 = 0.42$ .

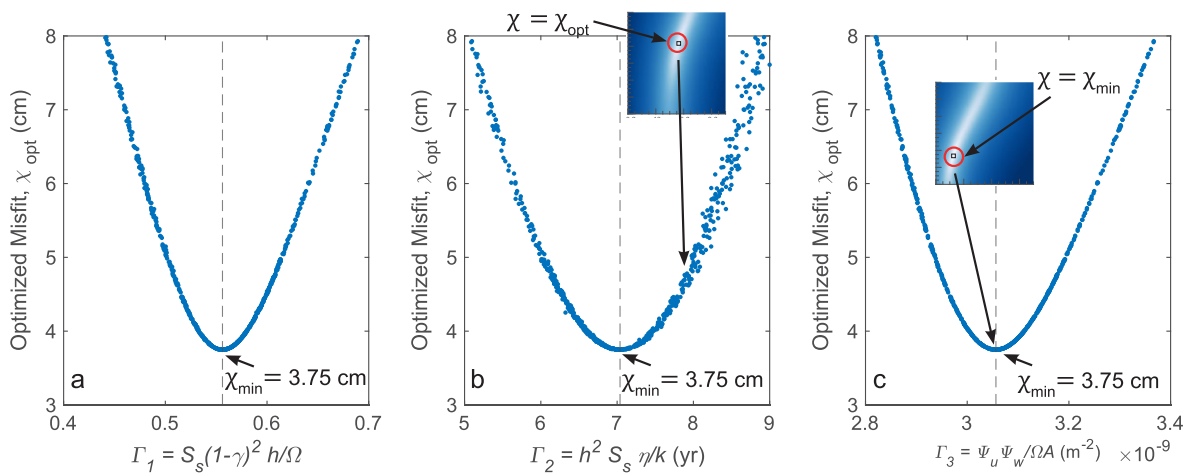


**Figure C3.**  $\chi_{\text{opt}}$  from a random search of parameter space. Three combinations of parameters, defined in Appendix C as  $\Gamma_1$ ,  $\Gamma_2$  and  $\Gamma_3$ , are plotted against  $\chi_{\text{opt}}$  in (a), (b) and (c), respectively. The blue and white thumbnails in (b) and (c), respectively show the loci of  $\chi_{\text{opt}}$  and  $\chi_{\text{min}}$  in  $S_s$ - $\eta/k$  space. Each blue point corresponds with one of these  $\chi_{\text{opt}}$  and associated with a unique combination of parameters and corresponding values of  $S_s$  and  $\eta/k$ . The lowest misfit  $\chi_{\text{min}} = 3.75$  cm is only associated with specific parameter combinations.